

June 24 and 25, 2021



**Bioengineering Institute of California**

Ten campuses united as one, learning and growing together



# University of California Systemwide Bioengineering Symposium

Bioengineering's role in the Covid19 era: Education, Discovery, Translation

SYMPOSIUM CHAIRS: PROF EDUARDO SILVA AND PROF  
CHEEMENG TAN





**Thursday**

Time	Event
9.00am	<b>Opening Remarks</b> Director Bioengineering Institute of California, Prof. Scott Simon (UC Davis) Chancellor Gary May (UC Davis)
9.15 - 10am	<b>Plenary lecture</b> <u>Chair:</u> Dr. Walt Baxter (Medtronic) <u>Invited Speaker:</u> Erik Engelson (Lucira Health) " <i>Bioengineering as a Career Launchpad, and the Lucira Health Molecular Covid Test</i> "
10.05 - 10.50am	<b>Session: Clinical Experiences for Bioengineers</b> <u>Chair:</u> Dr. James Kovach (UC Davis) <u>Invited Speaker:</u> Prof. Deborah Spector (UC San Diego) " <i>GEM - Galvanizing Engineering in Medicine at UCSD</i> " <u>Invited Speaker:</u> Prof. Scott Simon (UC Davis) " <i>Clinical physiology for undergraduates: immersive quarter @Aggie Square</i> "
*10.55 - 11.25am*	<b>Rapid-Fire Session - Hot Topic in Bioengineering</b> <b>Session Chair: Canary Meyer</b> The session will be conducted in a separate Zoom Meeting: <a href="https://ucdavis.zoom.us/j/5386151701?pwd=cmlW9PMDVDZkNmbGxBTE1rdnNBUT09">https://ucdavis.zoom.us/j/5386151701?pwd=cmlW9PMDVDZkNmbGxBTE1rdnNBUT09</a> , Passcode: 95616
	<b>Biomedical Imaging</b> <b>Rapid-fire Chair: Emmet Francis</b> <ol style="list-style-type: none"><li>1. Carlotta Trigila (UC Davis) "<i>Cerenkov photons polarization for improving optical simulation accuracy using the LUTDavis Model</i>"</li><li>2. Stephen Hsieh (UC Riverside) "<i>Near Field Electrospun M13 Virus-based Optical Resonator Biosensors</i>"</li><li>3. Hanna Koster (UC Davis) "<i>Surface-Enhanced Raman Scattering of Extracellular Vesicles for Cancer Diagnostics Despite Isolation Dependent Lipoprotein Contamination</i>"</li></ol>
	<b>Cellular Engineering</b> <b>Rapid-fire Chair: Luis Contreras-Llano</b> <ol style="list-style-type: none"><li>1. Sarah Stokes (UC Davis) "<i>Cellular therapy for in utero repair of myelomeningocele: a decade of translational bioengineering</i>"</li><li>2. Nastaran Abbasizadeh (UC Merced) "<i>Characterization of Microenvironmental Changes to the Bone Marrow after Cytotoxic Conditioning</i>"</li><li>3. Jeffrey Pham (UC Santa Barbara) "<i>The Effects of Cryopreservation on the Contractile Properties of Human iPSC Derived Cardiomyocytes</i>"</li></ol>
	<b>Molecular and BioMaterial Engineering</b> <b>Rapid-fire Chair: Tanner Henson</b>

	<ol style="list-style-type: none"> <li>1. Marcus Deloney (UC Davis) <i>"Peptide conjugated, surface modified hollow nanoparticles restore functionality to ex vivo osteoarthritic cartilage"</i></li> <li>2. Rama Reddy Goluguri (UC Merced) <i>"Tuning an engineered fold switching protein"</i></li> <li>3. <i>"A Pneumatic Random-Access Memory for Controlling Soft Robots"</i> Shane Hoang (UC Riverside)</li> </ol>
	<p><b>Computational Bioengineering</b>  <b>Rapid-fire Chair: Jung Hoo Kwon</b></p> <ol style="list-style-type: none"> <li>1. Shreya Shriram (UC Merced) <i>"Cell Detection in the Cleared Thymus using Machine Learning"</i></li> <li>2. Jie Shen (UC Irvine) <i>"Dynamic Finite Element Analysis of Crack Detection for Maxillary Second Bicuspid using Percussion Loading Conditions"</i></li> <li>3. Marc Creixell (UC Los Angeles) <i>"Motif-based peptide clustering improves phosphoproteome analysis"</i></li> </ol>
	<p><b>Tissue Engineering</b>  <b>Rapid-fire Chair: Sabrina Mierswa</b></p> <ol style="list-style-type: none"> <li>1. Alonso Torres (UC San Francisco) <i>"Glucose Clearance of an Intravascular Bioartificial Pancreas in a Diabetic Porcine Model"</i></li> <li>2. Karcher Morris (UC San Diego) <i>"Tissue Heat Transfer During Cardiac Radiofrequency Ablations"</i></li> <li>3. Joel Finbloom (UC San Francisco) <i>"Engineering Material Biointerfaces to Advance the Treatment of Cystic Fibrosis Lung Infections"</i></li> </ol>
11.30am - 12.15pm	<p><b>Session: Pandemic - Vaccine/Immunology/Diagnostic</b>  <b>Chair:</b> Prof. Stephanie Seidlits (UC Los Angeles)  <b>Invited Speaker:</b> Prof. Nisarg Shah (UC San Diego) <i>"Modulating Inflammation in Autoimmune Disease"</i>  <b>Selected Speaker:</b></p> <ol style="list-style-type: none"> <li>1. Nina Butkovich (UC Irvine) <i>"Immune-activating agonists in protein nanoparticle cancer vaccines"</i></li> <li>2. Alex Phan (UC San Diego) <i>"Portable Ophthalmic Instrument for Remote Self-Examination During COVID-19"</i></li> <li>3. Xiao Huang (UC San Francisco) <i>"Precise control of immune modulation using DNA scaffold-medicated biomaterial functionalization"</i></li> </ol>
12.20 - 1.30pm	<p><b>Shu Chien Early Career Award lectures</b>  <b>Chair:</b> Prof. Scott Simon</p> <ol style="list-style-type: none"> <li>1. Aaron Streets (UC Berkeley) <i>"Quantifying cellular identity with multimodal single cell analysis"</i></li> <li>2. Gao Liang (UC Los Angeles) <i>"Ultrafast bioimaging: seeing faster at microscopic scales"</i></li> <li>3. Seth Shipman (UC San Francisco) <i>"Hijacking Microbial Parts to Build New Molecular Technology for Human Disease"</i></li> </ol>

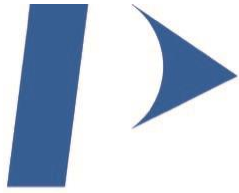
1.30 - 1.35pm	<b>Closing 1<sup>st</sup> day</b>
---------------	-----------------------------------

## Friday

Time	Event
9.00 - 9.55am	<p><b>Plenary lecture: Innovations in Bioengineering Education</b>  <u>Chair:</u> Prof. Jennifer Choi (UC Davis)  <u>Invited Speaker:</u> Prof. Ann Saterbak (Duke University) "<i>Education Bioengineers - Innovations and Opportunities</i>"</p>
*10.00 - 10.45am*	<p><b>Roundtable: Future of Careers in Bioengineering</b>  <u>Chair:</u> Dr. Walt Baxter (Medtronic) and Prof. Song Li (UC Los Angeles)  The roundtable will be conducted in a separate Zoom Meeting:  <a href="https://ucdavis.zoom.us/j/5386151701?pwd=cmlWaW9PMDVDZkNmbGxBTE1rdnNBUT09">https://ucdavis.zoom.us/j/5386151701?pwd=cmlWaW9PMDVDZkNmbGxBTE1rdnNBUT09</a>, Passcode: 95616</p>
	<p><b>Trends and Career Opportunities in BioPharma</b>  <u>Chair:</u> Prof. Aijun Wang (UC Davis)  <u>Panelists:</u> Dr. Linda Narhi (Amgen), John Maroney (Alessa Therapeutics), Dr. Eric Fallon (Genentech), and Dr. Dana Andersen (Denali)</p>
	<p><b>Trends &amp; Career Opportunities in the Biomedical Industry</b>  <u>Chair:</u> Don Chigazola (Retired Director of Operations, Medtronic Cardiovascular)  <u>Panelists:</u> Dr. Kevin Francis (Perkin Elmer), Mark Wang (Illumina), Jeffrey Clark (Medtronic)</p>
	<p><b>Future Trends in Foundation Investments</b>  <u>Chair:</u> Dr. Tom Skalak (Joe and Clara Tsai Foundation)  <u>Panelists:</u> Prof. Stephen Quake (CZI Biohub and Stanford University) and Dr. Lynda Stuart (Bill and Melinda Gates Foundation)</p>
10.50 - 11.35am	<p><b>Session: Future of BME research</b>  <u>Chair:</u> Prof. Cheemeng Tan (UC Davis)  <u>Invited Speaker:</u> Prof. Ronke Olabisi (UC Irvine) "<i>Combining 7th Century Insights with 21st Century Technology to Control Bone Formation and Involve Students from Around the World</i>"  <u>Selected Speaker:</u></p> <ol style="list-style-type: none"> <li>1. Tomas Gonzalez-Fernandez (UC Davis) "<i>Extracellular Matrix Enriched Spheroids for Enhanced Mesenchymal Stromal Cell Survival, Differentiation and Healing of Critically Sized Segmental Bone Defects</i>"</li> <li>2. Farnaz Mohammadi (UC Los Angeles) "<i>Drug Response Universally Drives Cell Cycle Pseudo-Synchronization Due to Phase Transit Times</i>"</li> <li>3. Sachin Govil (UC San Diego) "<i>Biventricular Shape Markers in Repaired Tetralogy of Fallot: Associations with Pulmonary Valve Replacement</i>"</li> </ol>
11.40am - 12.25pm	<p><b>Roundtable: Promoting Diversity, Equity, and Inclusion in Bioengineering</b></p>

	<p><u>Chair</u>: Prof. Tejal Desai (UC San Francisco) and Prof. Beth Pruitt (UC Santa Barbara)</p> <p><u>Invited Speaker</u>: Prof. Naomi Chesler (UC Irvine)</p>
12.30 - 1.25pm	<p><b>Keynote</b></p> <p><u>Chair</u>: Prof. Eduardo Silva (UC Davis)</p> <p><u>Invited Speaker</u>: Prof. Donald Ingber (Harvard University) <i>"Human Organ Chips: Clinical Mimicry in Preclinical Models"</i></p>
1.30 - 1.35pm	<p><b>Award Session</b></p> <p>Best Rapid-Fire Presentation, Best Oral Presentation, Shu Chien Early Career Award</p>
1.35 - 1.40pm	<p><b>Closing</b></p>

# Thank You to Our Sponsors



**PerkinElmer**<sup>®</sup>  
*For the Better*



**ALESSA**  
THERAPEUTICS

# Medtronic

Further, Together



*Shu Chien Early Career  
Lecturer Award*

*Bioengineering Institute of California*

Sponsored by a generous gift from Erik  
Engelson (CEO Lucira Health)



**Bioengineering Institute of California**

Ten campuses united as one, learning and growing together



# Engineering Material Biointerfaces to Advance the Treatment of Cystic Fibrosis Lung Infections

Authors: Joel A. Finbloom\*,<sup>1</sup> Michelle A. Yu,<sup>2</sup> and Tejal A. Desai<sup>1</sup>

<sup>1</sup>Department of Bioengineering and Therapeutic Sciences, University of California, San Francisco, CA 94158

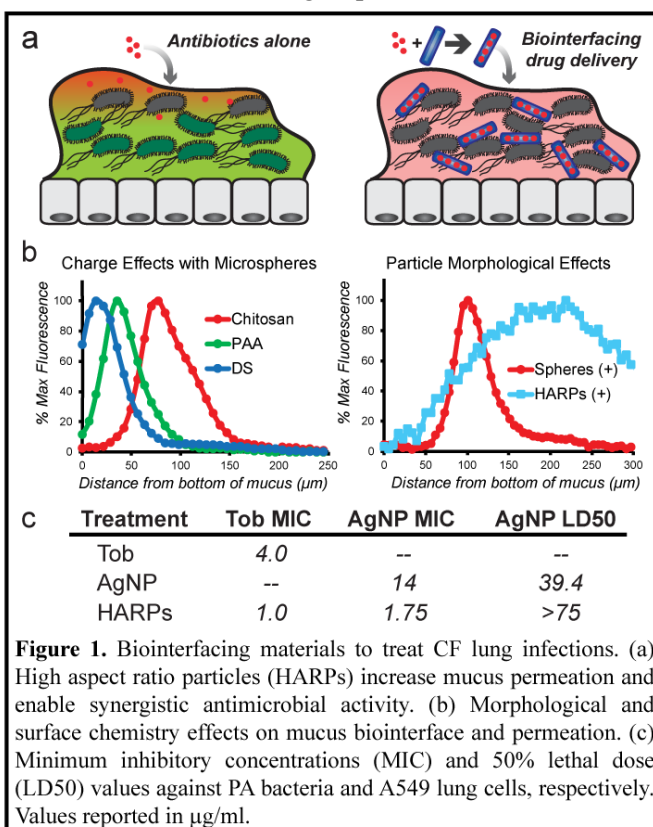
<sup>2</sup>Division of Pulmonary and Critical Care Medicine, University of California, San Francisco, CA 94143

**Introduction:** A cardinal feature of Cystic Fibrosis (CF) lung disease is bacterial colonization with multidrug-resistant pathogens such as *Pseudomonas aeruginosa* (*PA*). An important approach to overcoming resistant bacterial infections is treatment with synergistic antimicrobials. However, it is currently difficult to deliver multiple antibiotics at therapeutic concentrations to the same site of infection. Treatment of CF lung infections is also severely hampered by the thick and dehydrated mucus found in CF patient lungs, which limits mucus permeation and stability of antimicrobials. Antimicrobial drug delivery strategies could be greatly improved by engineering the material biointerface of drug carriers to enable improved lung adhesion, mucus permeation, and bacterial biofilm infiltration. To address these critical needs, we are engineering the physicochemical properties of antimicrobial-loaded micro and nanoscale materials to investigate how the morphologies and surface chemistries of these materials influence their biointerfaces and subsequent antimicrobial activities. By permeating mucus barriers, adhering to lung tissues, and delivering synergistic antimicrobials as well as mucolytic agents, we anticipate that these biointerfacing drug carriers will improve antimicrobial activity against CF pathogens (Fig. 1).

**Materials and Methods:** Particles were fabricated from poly(caprolactone) (PCL) polymers using a nanotemplating approach to yield rod-like high aspect ratio particles (HARPs) or by using precipitation to yield spherical PCL microparticles. Drug carriers were functionalized using layer-by-layer (LbL) electrostatic assembly to enable tunable surface chemistry display as well as antimicrobial drug loading. Silver nanoparticles (AgNPs) and tobramycin antibiotics (Tob) were the chosen antimicrobials for this study, as they have demonstrated synergistic antimicrobial activities. Antimicrobial activity and biocompatibility were assessed *in vitro* against laboratory strain *PA14* and A549 lung cells, respectively. *In vivo* activity was assessed in C57BL/6 wildtype mice infected with *PA14* in the lung followed by intratracheal instillation of treatment groups. Mice were sacrificed 6 or 24 h post-treatment, and lung bacteria were quantified along with lung neutrophil and white blood cell counts. Mucus permeation studies were conducted using microscopy analysis of fluorescently labeled particles incubated with a CF mucus mimic.

**Results and Discussion:** We observed increased mucus permeation with positively charged HARPs when compared to positive or negative microspheres, demonstrating the influence of surface charge and particle morphology on the mucus-material biointerface (Fig. 1b). Tob and AgNPs were loaded via LbL with high loading efficiencies, and HARPs demonstrated synergistic antimicrobial activity against *PA* bacterial strains and reduced off-target AgNP cytotoxicity against A549 lung cells (Fig. 1c). Preliminary *in vivo* studies demonstrated antibacterial activity of AgNP-loaded HARPs and studies are ongoing to assess the antimicrobial activity of AgTob-HARPs in mouse models. Using intravital lung microscopy, we observed HARPs present in peripheral lung alveoli co-localized with bacterial colonies, suggesting bacterioadhesive properties.

**Conclusions:** Taken together, these studies are providing immense insight into methods for engineering material biointerfaces to overcome delivery barriers for the treatment of CF lung infections. Current and future work is focused on evaluating the antimicrobial activity of AgTob-HARPs using *in vitro* biofilm models and mouse models of lung infection, as well as evaluating combined mucolytic and antimicrobial delivery with HARP drug carriers.



# Surface-Enhanced Raman Scattering of Extracellular Vesicles for Cancer Diagnostics Despite Isolation Dependent Lipoprotein Contamination

Hanna J. Koster<sup>1,\*</sup>, Tatu Rojalín<sup>1</sup>, Alyssa Powell<sup>1</sup>, Dina Pham<sup>1</sup>, Rachel R. Mizenko<sup>1</sup>, Andrew Birkeland<sup>2</sup>, Randy P. Carney<sup>1</sup>

<sup>1</sup>Department of Biomedical Engineering, University of California, Davis, Davis, CA

<sup>2</sup>Department of Otolaryngology – Head and Neck Surgery, University of California, Davis, Sacramento, CA

**Introduction:** Extracellular vesicles (EVs) are nanoscale packages shed by all cells and are important in cell-to-cell communication. Given that released EVs exhibit composition reflective of their parent cells in response to local external stimuli, they represent a rich source of potential biomarkers with great potential for clinical application. Yet many challenges remain before that potential can be reached, especially in the choice of EV isolation methodology, which has a known effect on the quality and content of the isolated product. In addition to vesicles, isolates may contain a variety of additional nanoscale biomolecular assemblies. There is no consensus on the expected concentration range of each particle type present in a given biofluid, since abundance is not predictable and influenced by a number of parameters, such as age, sleep, exercise, diet, and disease burden. This study focuses on quantifying extent of contamination in EV isolates by lipoprotein, which represent a major fluctuating source of nanoscale particles in human biofluids.

**Materials and Methods:** In this study we utilized surface-enhanced Raman scattering (SERS) to quantify the extent of lipoprotein contamination in a representative clinical dataset of EV isolates purified from plasma of head and neck cancer patients and healthy controls. We varied isolation methods between ultracentrifugation (UC), density gradient (DG), size-exclusion chromatography (SEC), and a combination of UC+SEC to assess the effect on lipoprotein vs. EV content. EVs were characterized using nanoparticle tracking analysis (NTA) to determine size and concentration, single particle interferometric reflectance imaging sensing (SP-IRIS) to confirm the presence of common EV-sequestered tetraspanins, and transmission electron microscopy (TEM) to visualize the EV and lipoprotein morphology. Samples were compared using principal component analysis (PCA) which reduces the dimensionality of Raman spectral datasets.

**Results and Discussion:** We found that the type of lipoproteins co-isolated with a given EV preparation varied depending upon the technique that was used. EVs isolated by SEC

grouped more consistently at the same locations as similarly sized lipoprotein, while EVs isolated by UC and DG shared more overlap lipoprotein in the same density range. A protocol of subsequent UC and SEC largely eliminated lipoprotein contamination. Therefore, if striving for purer EV samples to use in research experiments, a dual isolation method may be the most effective at removing these contaminating components. We also devised four machine learning approaches in order to evaluate the cancer detection and diagnostics capabilities of the studied SERS platform. In terms of cancer diagnostics, the best overall performance (accuracy = 98.3%) was achieved using the DG isolation method and a PCA-QDA discriminant classifier with PC1-PC3 scores as input features (**fig. 1**). However, SEC and UC isolations also achieved accuracies of 97.8% and 98%, respectively.

**Conclusions:** Our SERS platform was sensitive enough to tease out cancer-specific signatures that remained unaffected by the presence of additional co-isolated biomolecules, showing that the label free diagnostic ability was effective across many different sample preparations. However, some limitations remain. We analyzed a small dataset from head and neck cancers, and it is not clear how generalizable our finds are to other cancers and disease types. Also, there are many other types of contaminants besides lipoprotein in human biofluids that can pollute SERS spectra, whose influence will need to be investigated in future studies.

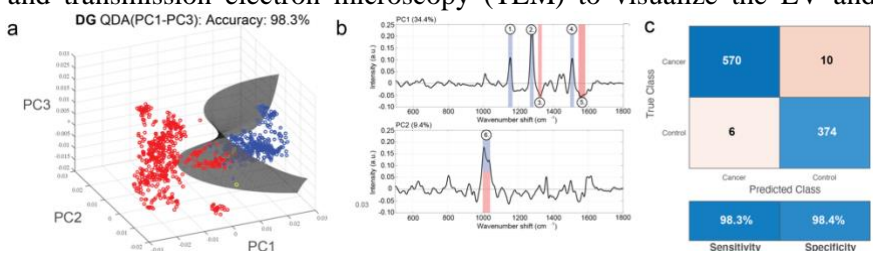


Figure 1: (a) EVs isolated from cancer (red circles) and non-cancer (blue circles) by DG. (b) Loadings for the first two PCs with annotated peaks highlighting driving factors for cancer features. (c) Confusion matrix including sensitivity and specificity.

# Cerenkov photons polarization for improving optical simulation accuracy using the LUTDavis Model

Carlotta Trigila<sup>1\*</sup>, Emilie Roncali<sup>2</sup>

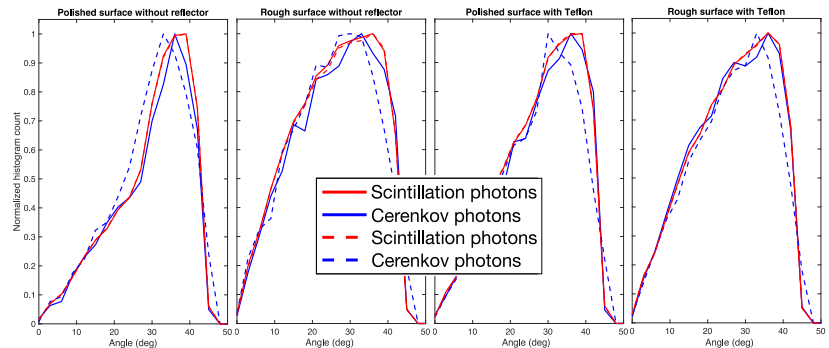
<sup>1</sup>Department of Biomedical Engineering, University of California Davis, Davis, CA, United States of America,

<sup>2</sup>Department of Radiology, University of California Davis, Davis, CA, United States of America

**Introduction:** Cherenkov photons have distinctive features from scintillation photons. Among them is their polarization: their electric field is always at a right angle to the direction of propagation of light and parallel to the plane of incidence. Scintillation photons are instead considered unpolarized. This study aims at understanding and optimizing the reflectance of polarized Cherenkov photons for optical Monte Carlo simulation of scintillation detectors. The Cherenkov characteristics were implemented inside the previously developed look-up-table Davis model of crystal reflectance. Then, optical Monte Carlo simulations using GATE were performed to show the effect of Cherenkov features on the photons' momentum at the photodetector face, using two surface finishes, with and without reflector and several crystal geometries.

**Materials and Methods:** In the LUT model of crystal reflectance, the photon's probability to be reflected or refracted by the surface is evaluated using Fresnel equation for unpolarized photons. This equation worked well to generate the *Unpolarized Photons LUTs*. Fresnel equations were modified to account only for the p-polarization contribution when generating *Cerenkov LUTs*. We computed LUTs for BGO polished and rough surfaces. They were merged into a *Scintillation-Cerenkov LUT* to account for scintillation and Cerenkov photon reflectance simultaneously. In GATE, we used a 511 keV back-to-back source centered between two 3x3 mm<sup>2</sup> BGO crystals. Thicknesses from 5 mm to 25 mm were tested. Arrangements with the photodetector (geometrical and quantum efficiency set to 1) placed in front or at the back of the crystals were compared. We separately used the *Unpolarized Photons LUTs* or merged *Scintillation-Cerenkov LUTs* on all crystal surfaces (polished-grease for the photodetector face; polished/rough with and without reflector for the edges). We modified Geant4/GATE source code to account for scintillation and Cerenkov photons simultaneously. We studied the distribution of the detected photons' incident angle on the photodetector face, estimated from their momentum before detection and the surface normal.

**Figure 1: Distribution of the detected photons' incident angle on the photodetector face for several simulated configurations. In bold, the scintillation and Cerenkov photons distribution when using Unpolarized LUTs. The dotted lines show the results when using the Scintillation-Cerenkov LUTs.**



**Results and Discussion:** Figure 1 shows the normalized distribution of the detected photons' incidence angles on the photodetector face. Photons arriving with an angle lower than  $\sim 42^\circ$  (critical angle for an BGO/grease interface) undergo transmissions on the photodetector face and are detected. All distributions steeply decrease around this angle. After, photons experience internal reflections. The scintillation photons distributions are the same when using the *Unpolarized LUTs* or *Scintillation-Cerenkov LUTs* (red lines), while the detected Cerenkov photons distributions (blue lines) show a shift towards lower incident angles in all configurations. The behavior is expected from a change in Cerenkov reflectance in the *Scintillation-Cerenkov LUTs*. Similar results are obtained with other thicknesses (not shown).

**Conclusions:** In this work, we presented the implementation of Cerenkov polarization inside the previously developed LUT Davis model. Monte Carlo simulations using GATE have been carried out. We showed that Cerenkov photons physical features integrated into the LUTs changed the photons momentum in several configurations. Considering the physical characteristics of scintillation and Cerenkov photons separately during the LUTs generation is thus important to run accurate optical Monte Carlo simulations. The changes in the photons' momentum are expected to affect the photon travel path and subsequently the detector timing performance in a way that is worth being thoroughly analyzed.

## Peptide conjugated, surface modified hollow nanoparticles restore functionality to ex vivo osteoarthritic cartilage

Authors: Marcus Deloney, Parssa Garoosi, Blaine A. Christiansen, PhD, Alyssa Panitch, PhD;  
University of California – Davis; Biomedical Engineering Graduate Group

**Objection/Goals:** Inhibiting the degradation of hyaluronic acid (HA) following joint trauma may halt the damaging cytokine cascade and prevent the resulting cyclic degradation of articular cartilage. Following joint trauma, inflammatory cytokine-recruited aggrecanase degrades aggrecan, thus exposing HA and allowing hyaluronidases to enzymatically degrade it. These degraded HA fragments then upregulate inflammatory cytokines which propagate the cyclic degradation of cartilage – leading to the development of osteoarthritis (OA). HA binding peptides (GAH) present a potential solution by binding to aggrecan depleted HA at the cleavage site – competitively inhibiting the enzymatic degradation of HA, however GAH itself is susceptible to proteolytic degradation in the extracellular space. We hypothesize that conjugating GAH to the surface of hollow nanoparticles (hNPs), termed GAH-hNPs, will protect GAH from enzymatic degradation while binding to HA in aggrecan depleted (AD) cartilage, thus restoring the compressive strength and functionality of ex vivo cartilage to healthy levels.

**Methods:** Hollow nanoparticles (hNPs) are composed of NIPAm, 2-acrylamido-2-methyl-1-propanesulfonic acid (AMPS), N,N'-bis(acryloyl)cystamine (BAC), and Acrylic Acid (AAc) and polymerized as previously described. *Peptide Modified NP Surface:* HA binding peptide, GAHWQFNALTVRGSG-Hydrazide (GAH-Hyd), was synthesized using Liberty Blue SEM and covalently bonded to the hNP using DMTMM conjugation at pH 4.5 and reacted for 60 h. *Ex vivo cartilage plugs:* Fetal bovine knees were obtained from Animal Technologies and plugs were taken using a 3 mm cork borer. Aggrecan was depleted using 0.5 (w/v)% trypsin and inflammation induced using 20 ng/ml IL-1 $\beta$ ; plugs were unstimulated and untreated (healthy), stimulated and untreated (AD), or treated on day 2 with 313  $\mu$ M or 1250  $\mu$ M of hNP or 65 GAH-hNP and cultured out to 12 days. *Compression:* Explant height was measured (Duratool) and compressive loads from 0 to 30% strain (at 5% intervals) with a 5  $\mu$ m/s ramp) and hold time of 30 s. Moduli were calculated with the slope of the linear fit equilibrium stress vs strain equation.

**Results:** Aggrecan depleted (AD) cartilage significantly lost compressive strength compared to healthy cartilage, 31.8  $\pm$  11.33 and 123.7  $\pm$  26.47 kPa, respectively at Day 6 and analogous at Day 12. The moduli of the plugs treated with 313  $\mu$ M hNP, 1250  $\mu$ M hNP, and 1250  $\mu$ M 65 GAH-hNP treated plugs at Day 6 and Day 12 were statistically analogous to AD. However, the modulus of 313  $\mu$ M 65 GAH-hNP at Day 6, 95.68  $\pm$  16.22 kPa, is statistically the same as healthy cartilage. At Day 12, the modulus of 313  $\mu$ M 65 GAH-hNP treated plugs is 79.66  $\pm$  21.88 kPa, and is analogous to the storage modulus of 313  $\mu$ M 65 GAH-hNP at Day 6, though statistically different than healthy cartilage.

**Discussion:** Binding to the aggrecan depleted HA within the ECM of cartilage protects the HA from further degradation, halting the progression of OA and retaining the mechanical properties of cartilage. The 313  $\mu$ M 65 GAH-hNP binds to exposed HA in aggrecan depleted cartilage plugs and restores the compressive strength to healthy cartilage plugs levels, Fig. 1. These data show the benefit of conjugating GAH to the surface of the hNP, as the AD plugs treated with unconjugated hNP, at both concentrations, have statistically the same moduli as untreated AD plugs. Moreover, extending the experiment out to Day 12, the plugs treated with 313  $\mu$ M 65 GAH-hNP maintain a higher modulus than untreated AD plugs, but still lower than healthy cartilage, while being statistically analogous to the plugs treated with 313  $\mu$ M 65 GAH-hNP at Day 6. These data give insight into when new treatments should be administered in the future. Our system has the potential to be the first therapeutic to treat the mechanical loss of function associated with cartilage degradation and prevent the progression of OA.

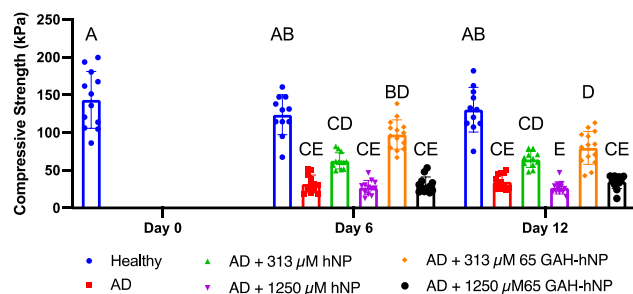


**Fig. 1:** A) Conjugation of GAH-Hyd to hNP at varying ratios of GAH to hNP B) Dynamic viscosity of 65 GAH-hNP particles at varying concentrations binds to HA

**Grant Numbers:** Research was supported by the National Institute of Arthritis and Musculoskeletal and Skin Diseases of the National Institutes of Health under award number R01AR065398 and the National Center for Advancing Translational Sciences, National Institutes of Health, through grant number UL1 TR001860 and linked award TL1 TR001861. The content is solely the responsibility of the authors and does not necessarily represent the official views of the NIH.

# Drug Response Universally Drives Cell Cycle Pseudo-Synchronization Due to Phase Transit Times

Farnaz Mohammadi<sup>1</sup>, Sean Gross<sup>2</sup>, Laura M. Heiser<sup>2</sup>, Aaron S. Meyer<sup>1</sup>

<sup>1</sup>Department of Bioengineering, University of California, Los Angeles, Los Angeles, California, USA

<sup>2</sup>Department of Biomedical Engineering, Oregon Health and Science University, Portland, Oregon, USA

**Introduction:** Accurately quantifying drug response is essential for designing effective anti-cancer agents. Though agents such as chemotherapies have known effects on the cell cycle, these have not been comprehensively characterized or analyzed using a unified quantitative model of pharmacological response. We build a computational framework to model cell cycle phase progression during drug response.

**Materials and Methods:** AU565 breast cancer cells were transduced with a fluorescent translocation cell cycle phase reporter. Nuclear or cytoplasmic localization of the reporter indicates cells in G<sub>1</sub> or S/G<sub>2</sub> phase, respectively (Fig 1A). The dynamic response of cells to five types of targeted or chemotherapy drugs was quantified employing a system of mean-field ordinary differential equations (ODE) to model the changes in the cell number in G<sub>1</sub> and S/G<sub>2</sub> phases over time. Quantified drug effects are fit to a Hill function, representing the sigmoidal shape of nonlinear dose-response curves. We used Bliss independence to calculate the additive combination of these five drugs.

**Results and Discussion:** Our analysis revealed that G<sub>1</sub> and S/G<sub>2</sub> cell cycle phase durations were gamma-distributed and that drugs necessarily lead to oscillations due to “pseudo-synchronization” when these cell cycle durations are extended. To account for the effect of gamma-distributed phase durations, we incorporated this delay effect through a mean-field system of ODEs using the “linear chain trick” (LCT) so that each phase is broken down into a series of sub-phases (Fig 1B). This model incorporating delay was able to accurately recapitulate the cell cycle response behavior to single-drug treatments (Fig 1C-E) and inferred parameters show how much these drugs extend/reduce the phase durations, and the chance of cell death in each cell cycle phase; for instance, lapatinib extends G<sub>1</sub> phase duration and induces a slight death effect in G<sub>1</sub>, and leaves S/G<sub>2</sub> phase almost unchanged (Fig 1F-G). We calculated drug combination predictions using our model and using only cell numbers as the reference and showed in most cases our model predictions were closer to their corresponding combination experiments (Fig 1H).

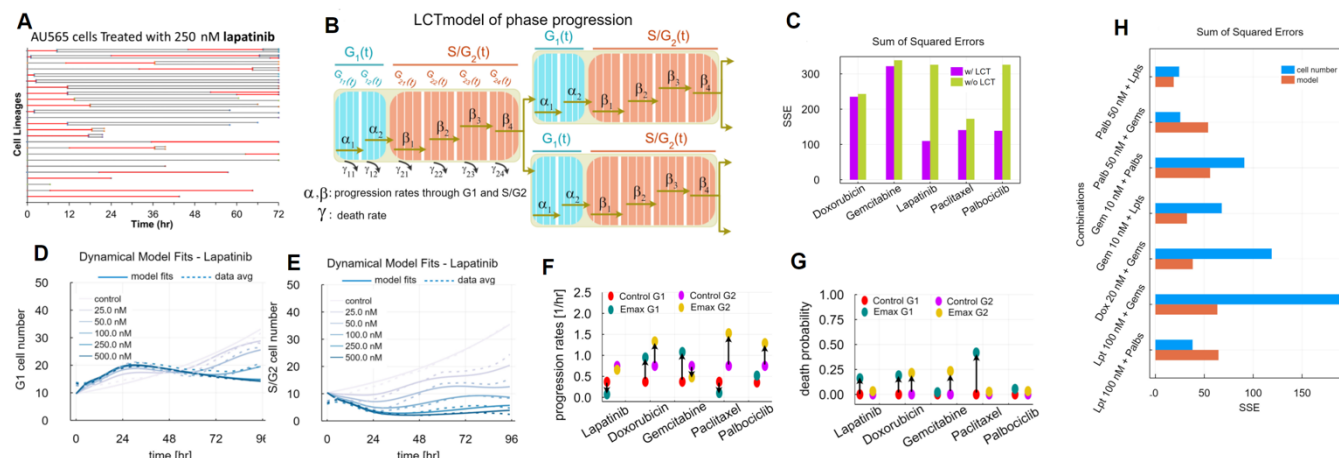


**Figure 1.** (A) Cell division/death in AU565 cells treated with 250 nM lapatinib over time. Cells in G<sub>1</sub> and S/G<sub>2</sub> phases are shown in gray and red lines, respectively. (B) Phase progression and cell death model;  $\alpha$  and  $\beta$  are progression rates within G<sub>1</sub> and S/G<sub>2</sub>, respectively;  $\gamma_{11}$  and  $\gamma_{12}$  are death rates in G<sub>1</sub>, and  $\gamma_{21}$ ,  $\gamma_{22}$ ,  $\gamma_{23}$ , and  $\gamma_{24}$  are death rates in S/G<sub>2</sub>. (C) The SSE for an ODE model with and without incorporating LCT. (D-E) Time-series data and simulations for cell number in G<sub>1</sub> and S/G<sub>2</sub> for lapatinib treatment. (F-G) Inferred cell cycle phase progression rates and death probabilities for all five drugs. (H) The SSE of predicting drug combination using our model compared to Bliss predictions based on cell numbers.

## Conclusions:

In total, we identified that all tested drugs have strong cell cycle-specific effects and cause cell cycle synchronization through a delay effect of the cell cycle. A dynamic model paired with live-cell reporters can help to analyze the influence of any drug on the dynamics of cell cycle phases. These findings could potentially lead to new optimized chemotherapy protocols using both timing and drug combinations.

## ***The Effects of Cryopreservation on the Contractile Properties of Human iPSC Derived Cardiomyocytes***

Orlando Chirikian, Jeffrey Pham, Beth Pruitt

**Introduction:** Cardiovascular diseases (CVDs) remains as the leading cause of death worldwide. Therefore, it is essential to advance our developmental understanding and modeling of cardiovascular disease so that we can better provide treatment to patients. However, modeling cardiovascular diseases, screening for drug toxicities, and understanding heart developmental processes remains a persistent challenge to the cardiovascular community due to their requirements of using large quantities of well-characterized and highly uniform populations of human cardiomyocytes. Although great strides have been made using animal models, there are key aspects of human cardiovascular physiology that these models fail to recapitulate. The utilization of Human-induced pluripotent stem cell-derived cardiomyocytes (hiPSC-CMs) has helped advance our ability to study the basic function of the heart and model cardiac diseases. However, modeling cardiovascular diseases, screening for drug toxicities, and understanding heart developmental processes remains a persistent challenge to the cardiovascular community due to their requirements of using large quantities of well-characterized and highly uniform populations of human cardiomyocytes. Many researchers source their hiPSC-CMs from collaborators or purchase frozen hiPSC-CMs, due to the complexities in stem cell culture and differentiation protocols. Generally, we assume the health of the cardiomyocyte remains if the cells reattach to their substrate and commence beating. However, very few have investigated the effects of cryopreservation on hiPSC-CM's functional and transcriptional health at the cellular/molecular level. Here we examine the effects of xeno-free cryopreservation on the functionality (contractility and calcium handling) and transcriptome of hiPSC-CMs from 6 healthy stem cell lines. Utilizing protein patterning methods to template physiological cell aspect ratios (7:1, length: width) in conjunction with polyacrylamide (PA) hydrogels, we are able to measure changes in force generation and calcium handling of single hiPSCs in pseudo physiological conditions (10kPa).

**Materials and Methods:** Induced pluripotent stem cell lines were obtained from the Stanford Cardiovascular Institute (SCVI) Biobank. All cell lines were propagated on Matrigel coated plates using feeder-free culture conditions (Essential 8) in standard environments consisting of 5% carbon dioxide at 37°C. hiPSC-CMs were then resuspended and frozen in one of the 3 cryopreservation media, CryoStor CS10, BamBanker, and CellBanker. Quantitative RT-PCR was performed on each hiPSC-CMs sample using Applied Biosystems SYBR Green kit. Traction Force Microscopy was performed using previously published methods and Single Cell Ca<sup>2+</sup> transient imaging was performed using Rhod4 calcium indicator. Functional data was analyzed using custom code.

**Results and Discussion:** Day 15 hiPSC-CMs (derived from 3 of the healthy iPSC lines) were replated after cryopreservation in confluent monolayers and cultured for an additional 13 days. Initial microscopy observation showed no striking difference between fresh and cryopreserved hiPSC-CMs other than increased cell death in the cryopreserved group as expected. Size measurements of single of hiPSC-CMs showed an increase in the spread area for cells that were cryopreserved compared to their fresh counterpart ( $728.0 \pm 19.0 \mu\text{m}^2 + 139.8 \mu\text{m}^2$  if frozen,  $p = 1.295\text{E-}7$ ,  $R^2 = 0.04331$ ). Traction Force Microscopy (TFM) measurements of single cell hiPSC-CMs displayed an increase in force generation in the cryopreserved population ( $29.5 \text{ nN} + 28.7\%$  if frozen,  $p = 0.001328$ ,  $R^2 = 0.01626$ ). Further inspection of the contractile dynamics depicted an increase in contraction velocity ( $350.5 \text{ nm/s} + 33.6\%$  if frozen,  $p = 3.945\text{E-}6$ ,  $R^2 = 0.03336$ ) and an increasing trend in relaxation velocity ( $254.6 \text{ nm/s} + 14.0\%$  if frozen,  $p = 0.06463$ ,  $R^2 = 0.005426$ ). Lastly, calcium handling of single hiPSC-CMs displayed delayed dynamics. These functional differences have been shown to be hallmarks of hiPSC-CM maturation. Transcriptome analysis demonstrates enhanced levels of well-known maturation genes SERCA2A, RYR2, and TNNT1 (ratio of isoform 3 compared to isoform 1).

**Conclusions:** Cryopreservation has provided a successful way of preserving biological material without integral alterations in the transcriptome or functionality of the cell. Our results demonstrate that cryopreservation selects for larger hiPSC-CMs and alters the functionality and transcriptome to resemble a more mature-like cell state measured by increased force generation and delayed calcium dynamics. This study informs the fields of basic science, regenerative medicine, and biological therapeutics of the effects of cryopreservation on hiPSC-CMs and may influence basic and translational scientists to reassess experimental design or take advantage of the maturation effects seen throughout the manuscript.

## Glucose Clearance of an Intravascular Bioartificial Pancreas in a Diabetic Porcine Model

Alonso Torres<sup>\*,a</sup>, Ana Santandreu<sup>a</sup>, Rebecca Shaheen<sup>a</sup>, Gregory Szot<sup>a</sup>, Nathan Wright<sup>a,b</sup>, Charles Blaha<sup>a,b</sup>, Rebecca Gologorsky<sup>a</sup>, Jarrett Moyer<sup>a</sup>, Eun Jung Kim<sup>a</sup>, Andrew Posselt<sup>a</sup>, and Shuvo Roy<sup>a,b</sup>

<sup>a</sup>University of California San Francisco, San Francisco, CA, 94158, USA

<sup>b</sup>Silicon Kidney LLC, San Francisco, CA, 94153, USA

**Introduction:** Type 1 diabetes (T1D) is caused by autoimmune destruction of  $\beta$  cells within pancreatic islets. Islet transplantation is a promising solution; however, donor shortage, need for immunosuppression, and risk of graft rejection limit widespread utility. Clinical trials suggest a minimum dose of 5,000 islet equivalents per kilogram of body weight (IEQ/kg) for portal vein islet infusions to achieve insulin independence. Bioartificial pancreas devices are designed to overcome requirements for immunosuppression, but most of them rely on diffusive transport, which hinders adequate solute delivery. In contrast, we are engineering an intravascular bioartificial pancreas (iBAP) that is enabled by Silicon Nanopore Membranes (SNM) and operates under convective transport. Our previous work with a small prototype established enhanced cell viability and glucose-insulin kinetics compared to its diffusion-based counterpart. In this study, we investigate the functionality of human islets in a scaled-up iBAP, which contains at least 24x more islets, implanted in an alloxan-induced diabetic pig (AP).

**Materials and Methods:** The iBAP (Figure 1A) consists of a polycarbonate housing with poly(ethylene glycol)-coated  $\sim$ 450 nm-wide pore SNM protecting freshly isolated adult human islets (UCSF Islet Core Facility) that were encapsulated in a 3% (w/v) agarose-microchannel matrix. Yucatan pigs (Sinclair Research – Auxvasse, MO),  $\sim$ 1-year-old, weighing 38-40 kg, were placed under anesthesia and vascular grafts were anastomosed to the inlet, outlet, and ultrafiltrate (UF) ports of the iBAP to their internal carotid artery, external jugular vein, and a secondary vein, respectively. First, sterile iBAP devices without islets were implanted in (n=3) healthy pigs (HP), to establish surgical technique and a baseline glucose clearance during an intravenous glucose tolerance test (IVGTT) by administering a 0.5 g/kg glucose bolus (Figure 1B). Next, in an AP, IVGTT established a diabetic glucose clearance curve (Post-diabetes) one day prior to device implantation. Then, an iBAP with 658 IEQ/kg was implanted, islets were stabilized for 90 min, and subjected to a 90-min IVGTT after implantation (iBAP). Blood extracted from the pigs was analyzed for glucose content using a glucometer (Accu-Chek Nano – Indianapolis, IN) and human and porcine C-peptide using ELISA kits (Mercodia – Uppsala, Sweden). The devices were implanted for up to seven days and the study was approved by the IACUC review committee at PMI Preclinical CRO, San Carlos, CA.

**Results and Discussion:** iBAP implantation was successful with no complications. During IVGTT of the iBAP implanted within the AP, porcine C-peptide remained as low as  $0.14 \pm 0.01$  ng/mL indicating effective diabetes induction and limited contribution in glucose clearance by the native pancreas. The average plasma human C-peptide concentration was  $0.71 \pm 0.06$  ng/mL, which is greater than the clinically accepted level (0.60 ng/mL) for T1D diagnosis. Lastly, the blood glucose decreased from  $> 600$  to 195 mg/dL, 90 minutes after glucose bolus, similar to that of the HP, demonstrating enhanced glucose clearance in comparison to the same pig's acute diabetic condition (Figure 1B).

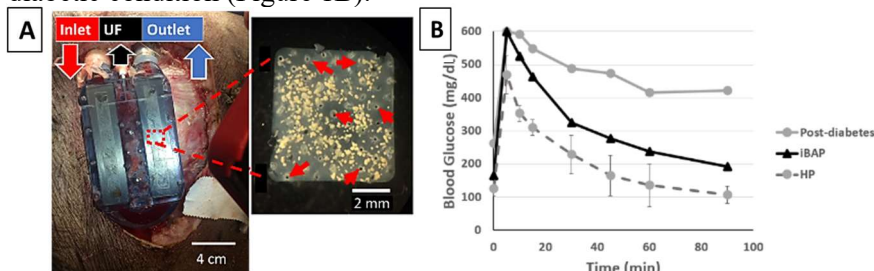


Figure 1: iBAP and Day 0 IVGTT: (A) Photograph of the iBAP in vivo and a close-up view of the islet scaffold with microchannels (red arrows) post-implant. (B) IVGTT with (n=3) healthy pigs (HP), an alloxan-induced pig (AP, Post-diabetes), and the AP with the device implanted (iBAP).

**Conclusions:** Clinically relevant C-peptide levels with the iBAP in the AP represent an important step towards clinical trials. Additionally, using this larger convection-based device provided enhanced glucose-insulin kinetics to the diabetic pig with a relatively small islet dose ( $< 700$  IEQ/kg) without immunosuppression. Future studies will target long-term experiments and an increased capacity to hold more islets within the iBAP.

**Acknowledgements:** This research was supported by the JDRF: 3-SRA-015-37-Q-R and the NIH/NIDDK Small Business Innovation Research (SBIR): R44DK104299. We thank Dr. Rachel Gurlin for her assistance.

# Extracellular Matrix Enriched Spheroids for Enhanced Mesenchymal Stromal Cell Survival, Differentiation and Healing of Critically Sized Segmental Bone Defects

Tomas Gonzalez-Fernandez (1), Alejandro J. Tenorio (1), Augustine M. Saiz (2), J. Kent Leach (1,2)

(1) Department of Biomedical Engineering, UC Davis, Davis, California, USA

(2) Department of Orthopaedic Surgery, School of Medicine, UC Davis Health, Sacramento, California, USA

**Introduction:** Effective strategies to mimic the cellular niche are necessary to promote stem cell survival and phenotype specification upon transplantation. The aggregation of mesenchymal stromal cells (MSCs) into three-dimensional spheroids enhances their survival, trophic factor secretion, and tissue-forming potential compared to monodispersed cells. Moreover, cell-secreted ECM represents a more complex platform to recapitulate the cues to guide stem cell fate versus individual matrix proteins or functional motifs. We hypothesized that the formation of MSC spheroids with cell-secreted ECM would enhance MSC viability, proliferation and osteogenic potential for the treatment of critically sized segmental bone defects.

**Materials and Methods:** Human bone marrow-derived MSCs were used in monolayer culture for ECM production or formed into spheroids for study. MSC-secreted ECM was incorporated into MSC spheroids *via* centrifugation. Incorporation efficiency was confirmed through biochemical and histological assays. MSC morphology and YAP/TAZ expression was observed by immunohistochemical staining. ECM-loaded spheroids were entrapped in 2% alginate hydrogels with low (DS2) and high (DS10) concentrations of RGD ligands. Differentiation was assessed through biochemical and histological analysis. The therapeutic potential of ECM-enriched MSC spheroids was evaluated in a critically sized femoral defect (6 mm). DS10 alginate constructs containing ECM-enriched MSC spheroids were implanted into the defect. Bone formation was analyzed at 4 and 12 weeks after implantation *via* microCT.

**Results and Discussion:** MSC spheroids formed with exogenous ECM possessed larger spheroid diameters, more tense actin cytoskeleton, increased YAP translocation to the nucleus and higher collagen and GAG content as the concentration of ECM increased from 0 to 7.5  $\mu\text{g}$  of ECM per spheroid (Fig. 1A-E). Moreover, ECM incorporation increased cell viability and reduced cell apoptosis. When entrapped in instructive alginate gels, ECM-laden spheroids in hydrogels of high RGD modification (DS10) exhibited greater DNA content, GAG and collagen (Fig. 1F-H), compared to non-loaded spheroids at the same ligand concentration or spheroids in gels with lower RGD concentration (DS2). Calcium accumulation was similar for MSC spheroids, regardless of the conditions (Fig. 1I). After implantation in a rat critically sized segmental bone defect, instructive alginate hydrogels containing ECM-enriched spheroids enhanced bone formation after 12 weeks of implantation compared to spheroids without ECM or spheroids entrapped in an alginate hydrogel with extrinsic ECM (Fig. 1J). ECM-enriched spheroids promoted full bridging of the defect as early as four weeks after implantation.

**Conclusions:** These results provide evidence that natural biomaterials are an effective addition to MSC spheroids to improve survival and instruct cell fate. These data have implications for improving the efficacy of autologous cell-based approaches to musculoskeletal repair using MSCs, a clinically relevant, safe, and readily accessible cell source.

**Acknowledgements:** This work was supported by the NIH award number R01 DE025475 and American Heart Association Postdoctoral Fellowship (19POST34460034) and the California Alliance for Minority Participation (CAMP) Scholarship.

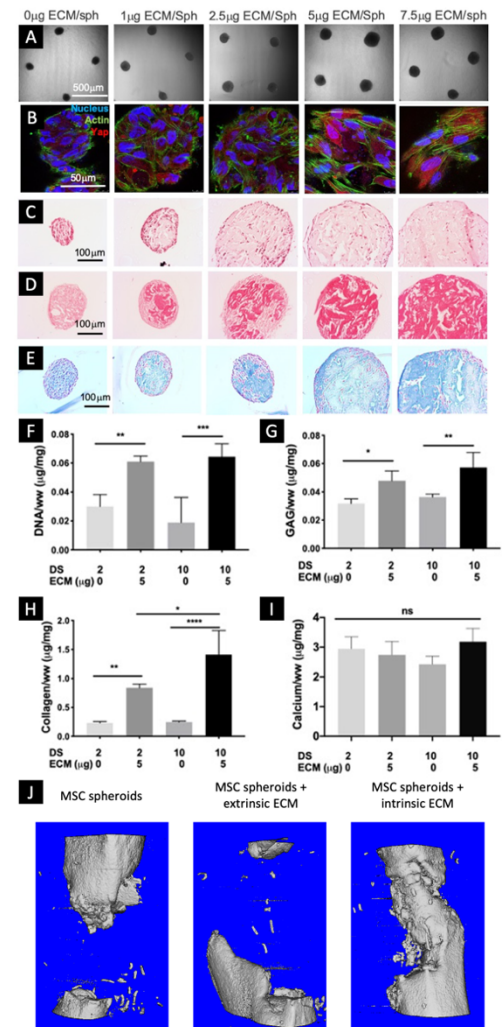


**Figure 1.** ECM-enriched spheroid characterization through microscopic imaging (A), staining for YAP/TAZ and cell cytoskeleton (B), H&E (C), collagen (D) and GAG (E) staining. Quantification of levels of DNA (F), GAG (G), collagen (H) and calcium (I) in osteogenically differentiated hydrogels containing ECM-enriched MSC spheroids or spheroids without ECM. (J) MicroCT images of femoral defects after 12 weeks *in vivo*.

## Cellular therapy for in utero repair of myelomeningocele: a decade of translational bioengineering

Sarah C. Stokes<sup>a\*</sup>, Christina M. Theodorou<sup>a</sup>, Jordan E. Jackson<sup>a</sup>, Edwin S. Kulubya<sup>a</sup>, Priyadarsini Kumar<sup>b</sup>, Christopher Pivetti<sup>b</sup>, Aijun Wang<sup>a,b</sup>, Diana L. Farmer<sup>a</sup>

<sup>a</sup> Department of Surgery, University of California-Davis, <sup>b</sup> Department of Biomedical Engineering, University of California-Davis

**Introduction:** Myelomeningocele (MMC), the most severe form of spina bifida, is a birth defect resulting from incomplete closure of the neural tube. The landmark Management of Myelomeningocele trial demonstrated that prenatal surgery to repair the MMC defect resulted in improved motor outcomes compared to postnatal surgery. Despite this benefit, there remains an ongoing clinical need, as only 55% of children who underwent *in utero* repair were able to walk at 30-months. Cell therapy is appealing for augmentation of *in utero* MMC repair as cell engineering is known to aid tissue repair. Over the past 10 years our laboratory engineered an optimal cell line and delivery vehicle for *in utero* repair and now are proceeding with a first in human clinical trial.

**Materials and Methods:** We aimed to provide a detailed evaluation of the progress from translational research to a clinical trial. Sheep studies, the gold standard animal model for *in utero* repair of MMC, evaluating cellular therapy conducted in our laboratory over the past decade were reviewed. Data extracted included cell type, vehicle for cellular delivery, motor outcomes, spinal histology, wound healing and cell persistence.

**Results and Discussion:** The first delivery vehicle investigated was a nanofibrous scaffold. Nanofiber scaffold alone did not induce inflammatory response or fibrosis in fetal sheep (n=2)(1). Human induced pluripotent stem cells from neural crest stem cells (iPSC-NCSCs) were then combined with hydrogel and spread onto the surface of nanofibrous scaffolds. Cells integrated into the spine of the fetal lambs (n=2), differentiated into neuronal lineage and persisted in lamb spinal cords(2). However, both delivery vehicle and cell therapy posed problems. Surrounding tissue adhered to the nanofibrous scaffold, which could potentially increase spinal cord tethering. iPSC-NCSCs have the potential to acquire new mutations and are not the safest cellular therapy option for a fetus. Fetal amniotic membrane (AM) was then evaluated, as it could potentially be an autologous therapy and has anti-inflammatory properties. AM alone was associated with increased spinal cord preservation(3). However, the majority of lambs repaired with amniotic membrane (n=3/4) had impaired wound healing of the overlying skin. AM was then combined with placental mesenchymal stromal cells engineered along a neurogenic pathway (ePMSCs) suspended in hydrogel, as PMSCs had been demonstrated to have immunomodulatory and neuroprotective properties. All lambs repaired with ePMSC and AM had decreased wound healing (n=2/2)(4). However, ePMSCs and AM improved lamb motor function and increased large neurons in the spinal cord compared to AM alone. Given the success of ePMSCs with AM, ePMSCs were then applied to the fetal spinal cord in a hydrogel mixture covered by a single ply extracellular matrix. ePMSCs delivered in this fashion were effective, with 4/6 lambs repaired with ePMSCs able to walk independently compared to 0/6 repaired with the delivery vehicle alone(5). While this was effective, before moving to a clinical trial, we needed to find a non-rat tail collagen derived delivery vehicle that was approved by the Food and Drug Administration (FDA) and would allow direct topical application of the cells to the fetal spinal cord. A commercially available extracellular matrix approved for dural repair (Duragen) was identified as a delivery vehicle that proved ideal for seeding and activating the ePMSCs. ePMSCs seeded on ECM were again demonstrated to be associated with improved motor function and increased large neuron density(6,7). ePMSC seeding density was then optimized through *in vivo* studies(6).

**Conclusions:** After a long journey of discovery, the combination product of ePMSCs seeded onto clinical grade ECM was identified as the optimal combination of effective cellular therapy on a functional delivery vehicle. This combination is safe, easy to apply surgically and provides evidence of neuroregeneration in animal models and is now approved for first in human clinical trials.

(1) Saadai P, J Pediatr Surg. 2011;46(12):2279-83. (2) Saadai, P, J Pediatr Surg. 2013;48(1):158-63. (3) Brown EG, J Pediatr Surg. 2014;49(1):133-7. (4) Brown EG, Fetal Diagn Ther. 2016;39(3):179-85. (5) Wang A, Stem Cells Transl Med. 2015;4(6):659-69. (6) Vanover M, J Pediatr Surg. 2019;54(1):75-9. (7) Kabagambe S, J Pediatr Surg. 2017. S0022-3468(17)30654-1

# Biventricular Shape Markers in Repaired Tetralogy of Fallot: Associations with Pulmonary Valve Replacement

Sachin Govil<sup>1\*</sup>, Charlene Mauger<sup>2</sup>, Xiaoyang Yu<sup>3</sup>, Sanjeet Hegde<sup>4</sup>, James C. Perry<sup>4</sup>, Alistair A. Young<sup>5</sup>, Jeffrey H. Omens<sup>1</sup>, Andrew D. McCulloch<sup>1</sup>

<sup>1</sup>Department of Bioengineering, University of California San Diego, USA

<sup>2</sup>Department of Anatomy and Medical Imaging, University of Auckland, NZ

<sup>3</sup>The Heart Institute, Rady Children's Hospital San Diego, USA

<sup>4</sup>Department of Pediatrics, University of California San Diego, USA

<sup>5</sup>Department of Biomedical Engineering, King's College London, UK

**Introduction:** Surgical repair of tetralogy of Fallot (TOF) often involves damage to the right ventricular (RV) outflow tract typically resulting in pulmonary valve impairment and subsequent pulmonary regurgitation (PR). Residual PR leads to progressive RV remodeling and plays an important role in long-term outcome. Patients with severe PR undergo pulmonary valve replacement (PVR) to reduce the risk of heart failure. However, the clinical decision on whether and when to perform PVR remains unclear. Current indications rely on global measures of ventricular volumes and masses but are widely debated, inconsistently applied, and lead to mixed outcomes. We aimed to test the hypothesis that specific markers of biventricular shape can discriminate differences in ventricular remodeling between repaired TOF patients that were and were not designated for follow-up PVR better than traditional clinical indices, that may be early markers of adaptive vs. maladaptive ventricular remodeling.

**Material and Methods:** In this cross-sectional retrospective study, biventricular shape models were fit to cardiovascular magnetic resonance images from 84 repaired TOF patients using diffeomorphic, non-rigid registration to manual contours drawn by an expert analyst. Deidentified datasets were contributed from multiple clinical centers with local IRB approval. A statistical atlas of end-diastolic (ED) shape was constructed using principal component analysis. Multivariate regression was used to quantify biventricular shape markers / clinical indices associated with subsequent intervention status (PVR vs. No-PVR), while accounting for differences in sex, time after primary repair, and body habitus. Significant correlations between biventricular shape markers / clinical indices and PVR status were assessed via ANOVA. K-means clustering was then used to test the ability of statistically significant biventricular shape markers / clinical indices to discriminate PVR status. The quality of clinical classification was evaluated using Matthews correlation coefficient (MCC).

**Results and Discussion:** Intervention status was significantly correlated with biventricular shape markers associated with RV apical dilation and left ventricular (LV) dilation (ED4,  $p < 0.001$ ), RV basal bulging and LV conicity (ED6,  $p < 0.02$ ), and pulmonary valve dilation (ED25,  $p < 0.002$ ). Intervention status was also significantly correlated with RV ejection fraction ( $p < 0.03$ ) and was non-significantly correlated with LV end-systolic volume index ( $p < 0.06$ ). Clustering analysis revealed that the aforementioned markers of biventricular shape were able to discriminate PVR status better than the aforementioned traditional clinical indices (MCC=0.49 and MCC=0.28, respectively). Upon further inspection, patients in the No-PVR group demonstrated increased RV apical dilation, which may be an adaptive type of remodeling, while patients in the PVR group demonstrated increased RV basal bulging, LV dilation, and LV conicity, which may be maladaptive types of remodeling.

**Conclusion:** Complex biventricular shape markers were able to discriminate differences between patients that were and were not designated for follow-up valve replacement better than traditional clinical indices, despite the fact that these indices are already used in clinical evaluation for the decision to perform PVR. These shape markers enable quantification of specific regional features of cardiac morphology that can provide mechanistic insight into adaptive vs. maladaptive types of ventricular remodeling that may be overlooked when relying solely on global ventricular measurements. In future studies, simulations of systolic mechanics will be performed to identify whether variations in ED geometry alone are direct determinants of dysfunction or if they may be indirect markers of altered myocardial contractility, or a combination of both.

## Motif-based peptide clustering improves phosphoproteome analysis

Marc Creixell<sup>1</sup>, Aaron S. Meyer<sup>1</sup>—UCLA, Department of Bioengineering

**Introduction** Cell signaling is regulated in part through a network of protein kinases. Dysregulation of kinase signaling is widespread in diseases such as cancer and is readily targetable through inhibitors of kinase enzymatic activity. Mass spectrometry-based analysis of kinase signaling can provide a global view of kinase signaling regulation but making sense of these data is complicated by its stochastic coverage of the proteome, measurement of substrates rather than kinase signaling itself, and the scale of the data collected. Here, we propose a combined data and motif clustering strategy (DDMC) that simultaneously clusters substrate peptides into similarly regulated groups based on their variation within an experiment and their sequence profile. We show that this can help to identify putative upstream kinases and supply more robust clustering. We apply this clustering to large-scale clinical proteomic profiling of 110 treatment-naïve lung adenocarcinoma (LUAD) tumors and 101 paired normal adjacent tissues (NATs) from the NCI's CPTAC LUAD study and identify conserved proteomic signatures of tumorigenicity, genetic mutations, and tumor immune infiltration. We propose that DDMC provides a general and flexible clustering strategy for phosphoproteomic data.

**Materials & Methods** We built a mixture model that probabilistically clusters phosphosites based on both their peptide sequence and abundance across samples. In each iteration, DDMC applies an expectation-maximization algorithm to optimize clusters that capture the average features of member sequences and their abundance variation. Clustering both the sequence and abundance measurements ensures that the resulting clusters are a function of both features, which we hypothesized would provide both more meaningful and robust clusters. The resulting clustering provides coordinated output that can be used in a few different ways. The cluster centers, by virtue of being a summary for the abundance changes of these peptides, can be regressed against phenotypic responses to establish associations between particular clusters and response. In parallel or independently, one can interrogate the resulting Position-Specific Scoring Matrices (PSSMs) to describe the overall sequence features of that cluster. This can be compared to other information such as experimentally generated specificity profiles of putative upstream kinases via Position Specific Scanning Libraries (PSPL), to infer upstream kinases.

**Results and Discussion** We first benchmarked and verified that DDMC clearly outperforms the use of standard methods such as the peptides' average, minimum signal, or constant zero to impute missing values. We then confirmed that DDMC correctly predicts AKT1 and ERK2 as upstream kinases of signaling clusters containing their experimentally validated substrates. Additionally, we found that incorporating the sequence information into the clustering criterion improves prediction of different phenotypes and indeed optimizes for the information content of both sequence motifs and phosphorylation behaviors. Finally, we comprehensively characterized those clusters that mostly contribute to explaining sample type (tumor vs NAT, **Figure 1**), STK11/EGFR/ALK mutational status, and tumor immune infiltration.

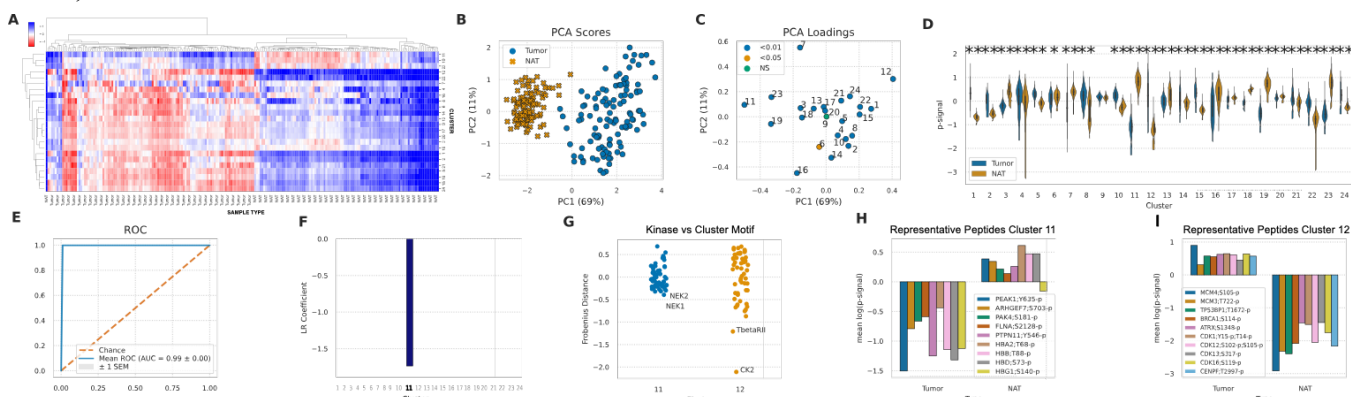


**Figure 1. Tumor vs NAT DDMC analysis** (A) Hierarchical clustering (B-C) PCA analysis of clusters (D) p-site abundance of tumor vs NAT (E) Logistic regression performance and weight (F) Kinase prediction (G) Upstream kinase prediction (H-I) Phosphorylation signal of representative peptides in clusters 11 and 12 in tumor vs NAT.

**Conclusion** Phosphoproteomic data provides information about both the sequence features and abundance of a peptide. DDMC simultaneously models both information sources despite the presence of missing values to identify signaling dysregulation common to tumors, specific genetic backgrounds, and tumor infiltration status.

## Tuning an engineered fold switching protein

Rama Reddy Goluguri<sup>\*1</sup>, Mourad Sadqi<sup>1</sup>, Luis Campos<sup>2</sup> and Victor Muñoz<sup>1</sup>

1- Department of Bioengineering & Center for Cellular and Biomolecular Machines (CCBM), University of California, Merced, CA. 2- National Biotechnology Center, CSIC, Darwin 3, Madrid 28049 Spain

**Introduction:** Some protein sequences that are at the brink of stability were known to exist in two different folds, a phenomenon termed as protein metamorphosis and the proteins referred to as fold switching proteins or metamorphic proteins. Nature utilizes fold switching to perform complex functions such as fusion of a virus to the host cell and controlling the circadian rhythms in cyanobacteria. Fold switching proteins are an attractive scaffold for designing the transducer of protein-based biosensors. This is because the affinity for the analyte of a fold-switch protein biosensor can be modulated by tuning the equilibrium between the two alternate folds. We previously engineered a protein fold switch in a naturally occurring stable protein CI2 by making several mutations that promote the emergence of an alternative, ancestral fold. In this study we tune the equilibrium population of the two folds by controlling the stability of the native fold by mutation, salt and temperature.

**Materials and Methods:** The N and C termini of the engineered CI2 protein are in close proximity in the native state, but they are far apart in the fold switched conformation. We designed a single molecule FRET experimental strategy to monitor the transition between the two folds at single molecule resolution. We labeled the N and C termini of the protein with Alexa 488 (Donor) and Alexa 594 (Acceptor) through the cysteines engineered at the two termini (Figure 1). This approach enables to monitor the transitions between the native and switched fold at the single molecule level using free diffusion confocal single-molecule fluorescence spectroscopy. These experiments produce time-stamped 2-color photon trajectories that can be analyzed using maximum likelihood methods to extract the dynamics of the fold switch transition.

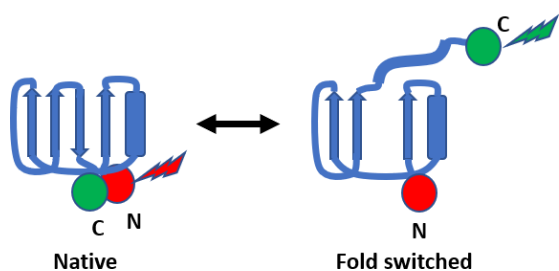


**Figure 1. Schematic diagram showing the two alternative conformations of engineered CI2 protein. The two termini were labeled with donor and acceptor fluorophores. As the protein diffuses through the confocal volume the fluorescence from donor and acceptor are used to monitor the interconversion between the two states.**

**Results and Discussion:** The equilibrium between the two conformations of the CI2 protein is found to be extremely sensitive to the solvent conditions, temperature and protein sequence. Point mutations that are known to destabilize the native fold were confirmed to increase the population of the switched fold in single molecules. Increase in temperature and denaturant (native destabilizers) were observed to favor the fold switched conformation, whereas increases in salt concentration are found to strongly stabilize the native fold, indicating that electrostatic screening is a major factor in tuning the native-switched fold equilibrium.

**Conclusions:** The marginal stability of metamorphic proteins results in a delicate tradeoff between two different structures. The observations we made in our engineered fold-switching CI2 helps understand the principles that govern this delicate balance. Our results help to understand the mechanism of protein fold switching phenomena which should prove tremendously useful for learning how to efficiently design fold switching variants of other natural proteins.

**Acknowledgements:** Funding was provided by National Science foundation (NSF-MCB-1616759), the CREST Center for Cellular and Biomolecular Machines (NSF-CREST-1547848), and the W.M. Keck Foundation.

# Dynamic Finite Element Analysis of Crack Detection for Maxillary Second Bicuspid using Percussion Loading Conditions

Jie Shen, Cherilyn Sheets and James C. Earthman

**Introduction:** Cracked and fractured teeth can arise due to teeth grinding, hard biting, gum disease and fatigue. Cracks may go unnoticed until a complete fracture occurs. By the time a reliable diagnosis is determined, a crack may well have propagated to the point where the tooth needs to be extracted. Clinical dentistry has been limited by a lack of diagnostic tools that detect cracks in teeth. However, quantitative percussion diagnostics (QPD) has demonstrated much potential in recent years for detecting and characterizing cracks in teeth. The goal of this research is to use finite element analysis (FEA) to better understand the complexity and patterns of force-time plots generated by QPD, mainly addressing how peaks are formed and how they are related to different crack types. The maxillary second bicuspid was examined with oblique and vertical crack. The significant findings of this research would be able to help dentists recognize the unknown crack conditions using QPD results, so that better diagnoses and treatments can be administered.

**Materials and Methods:** Finite element analysis (FEA) is able to simulate QPD testing by modeling, meshing, and simulating the mechanical response results for cracked teeth under percussion loading conditions. First, SOLIDWORKS is used to create the 3D model of the maxillary second bicuspid, based on computer tomography data including tooth geometries and sizes which were provided by eHuman, Inc. (Fremont, CA). There is a total of six SOLIDWORKS components in one model: enamel, dentin with empty pulp chamber, periodontal ligament, bone, and percussion rod. MSC Apex software is being used to create the meshes for the present 3D CAD tooth models. MSC Marc/Mentat (MSC Software, Newport Beach, CA) is being used to run the simulations after importing meshed tooth model. MSC Marc, a nonlinear FEA solver, was chosen because of its ability to model nonlinear material behaviors and transient environmental conditions, which allows for an accurate simulation under dynamic loading conditions.

**Results and Discussion:** Two vertical crack models in the maxillary second bicuspid with crack length 5mm and 8mm are compared. Both of them result in multiple peaks the force-time plot corresponding the sensor in the QPD percussion rod. First, it was found that longer vertical crack would result in a greater number of peaks with higher peak-to-valley ratios. This is due to the structure instability and crack face relative velocity changes. Second, it was found that peaks are a result of crack face oscillations. The first individual peak in both force-time plots is due to the initial contact between the tooth and percussion rod followed by deviation in the velocities of the two faces. Because of the oscillation, the two crack surfaces are eventually in contact as indicated by the red solid line in Figure 1. At the maximum force, the kinetic energy is fully exhausted, and then the overall force starts to decay.

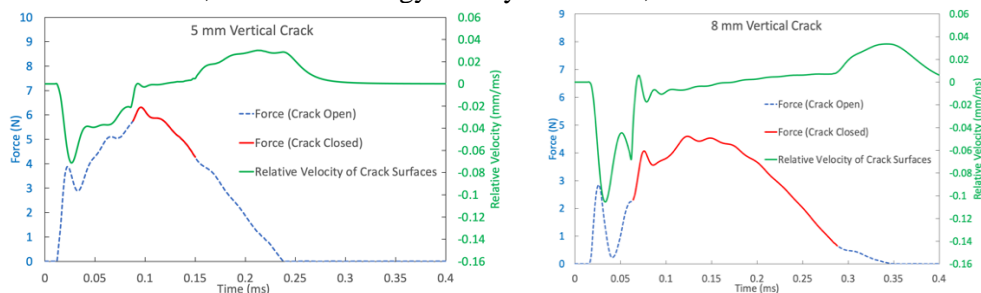


Figure 1: FEA Force - time plot in dashed blue (crack opening) and solid red (crack closing) for vertical crack in a maxillary second bicuspid with the crack length of 5 mm (left) and 8 mm (right). Relative velocity vs. time (in green) indicating the difference in the crack face velocities under percussion loading.

**Conclusion:** This present research examined the effects of oblique cracks and vertical cracks on the QPD response of a maxillary second bicuspid using FEA simulations. The 5mm and 8mm vertical crack force-time plots exhibit multiple peaks, and there are more peaks when the vertical crack is longer. Short and long oblique crack models also lead to the same findings. Relative velocity plots show that the additional peaks in the force-time plot are not necessarily caused by the crack closure. Rather, some peaks can be due solely to relative oscillations between the two crack faces.

## Immune-activating agonists in protein nanoparticle cancer vaccines

Nina Butkovich\*, Jo Anne Tucker, Edward L. Nelson, Szu-Wen Wang  
University of California, Irvine

**Introduction:** Cancer is the second leading cause of death in the United States, but current treatment options may lack efficacy or cause severe side effects. While immune checkpoint inhibitors have experienced recent clinical success against numerous cancer types, long-term remission is common. However, their combination with cancer vaccines is a promising avenue to facilitate immune system recognition of tumor-associated antigens. Our lab has previously shown success with a nanoparticle (NP)-based cancer vaccine, utilizing the internally and externally functional hollow E2 protein (composed of 60 identical subunits for a total diameter of ~25 nm).<sup>1</sup> Yet these previous studies utilized only a highly murine-activating DNA sequence, CpG 1826, and alternative agonists were not investigated. While bacterial-like DNA such as CpG 1826 may activate Toll-like-Receptor 9 (TLR9), viral ssRNA may activate an alternative receptor, TLR7. These current studies formulate E2 vaccines with the clinically-used bacterial-like DNA sequence, CpG 1018, or 20-mer ssRNA from HIV-1. This research suggests differential activation of two main dendritic cell (DC) sub-populations, the primary antigen-presenting cells of the body, through targeting of TLR7 or TLR9.

**Materials and Methods:** E2 protein NPs were expressed and purified, then conjugated to agonist via maleimide/aldehyde chemistry. Formulation characterization included dynamic light scattering, SDS-PAGE, and mass spectrometry to confirm NP uniformity and determine conjugation efficiency. Myeloid- or plasmacytoid-skewed murine bone marrow-derived dendritic cell cultures were generated *in vitro* through incubation with GM-CSF or hFlt3, respectively. Formulations or free agonist stimulated cells for 24 hr (37°C), and levels of activation were analyzed through flow cytometry following fluorescent staining of cell surface markers.

**Results and Discussion:** E2 has been successfully conjugated to CpG 1826, CpG 1018, and 20-mer ssRNA, with approximately 0.5 µg of each agonist internalized within 5 µg of intact E2. Encapsulation of TLR9 agonists within E2 elicited increased activation of myeloid dendritic cells (mDCs), though there was marginal or no response against encapsulated or free TLR7 agonists. In contrast, plasmacytoid dendritic cells (pDCs) were highly sensitive to both CpGs and 20-mer ssRNA, even before encapsulation. Myeloid DCs are efficient antigen cross-presenters to T cells, which may directly kill or help coordinate attack against infected or cancerous cells. Plasmacytoid DCs have exceptional ability to secrete pro-inflammatory cytokines at sites of inflammation, serving as especially important mediators of antiviral response.<sup>2</sup> The results of this ongoing study suggest that an E2 cancer vaccine may be synthesized to activate one or both DC subtypes, facilitating a tunable immune response.

**Conclusions:** These studies suggest that E2-based cancer vaccines can be formulated to differentially activate two murine dendritic cell sub-populations, vital in orchestrating targeted immune responses, through specific TLR activation. Our ongoing studies assess dosage responses and cytokine secretion of mDCs and pDCs.

**References:** 1-Molino, N., et al., *ACS Nano*. 2013; 7(11): 9743-9752. 2-Gulubova, M., *OAMJMS*. 2019; 7(19): 3324-3340.

# Near Field Electrospun M13 Virus-based Optical Resonator Biosensors

Stephen T. Hsieh<sup>1†</sup>, Joseph E. Cheeney<sup>1</sup>, Xi Ding<sup>2</sup>, Nosang V. Myung<sup>3</sup>, Elaine D. Haberer<sup>1,2\*</sup>

<sup>1</sup>Material Science and Engineering Program, University of California, Riverside, CA USA.

<sup>2</sup>Department of Electrical and Computer Engineering, University of California, Riverside, CA USA.

<sup>3</sup>Department of Chemical and Environmental Engineering, University of California, Riverside, CA USA.

**Introduction:** Polymer/virus-based biosensors are a compelling system for medical diagnostics, environmental monitoring, and food security. Typically, antibodies or aptamers are used as the bio-recognition element; however they can be costly and time-consuming to produce, lack stability under sensing or surface functionalization conditions, and be poorly oriented during functionalization rendering a fraction of receptor sites useless. In contrast, the M13 virus, a harmless and non-toxic filamentous bacteriophage, can be manufactured in large quantities through inexpensive infection of a bacterial host. Furthermore, it is durable over a large range of temperatures and pHs. Moreover, this combinatorial phage display workhorse can be genetically modified to display thousands of well-ordered, densely packed affinity peptide fusions with controlled orientation along its nearly one-micron length.

Recently published work<sup>1</sup> has demonstrated that electrospun polymer fibers can act as optical whispering gallery mode (WGM) resonators. These WGM resonators were shown to be highly sensitive, label-free refractive index sensors. To investigate a M13 WGM biosensor device, we electrospun polymer/M13 fibers capable of supporting WGM while maintaining the M13 bio-recognition properties for biosensing.

**Materials and Methods:** We used near-field electrospinning, a direct-write fabrication method utilizing an electric field, to create polyvinyl alcohol (PVA) WGM fiber resonators with incorporated M13 virus biorecognition elements. A streptavidin-binding phage functioned as a model bioreceptor to evaluate the response of the PVA/M13 WGM sensing platform. The surface concentration of M13 was evaluated via streptavidin-conjugated gold nanoparticle binding studies and x-ray photo spectroscopy (XPS). Rhodamine 6G (R6G) was then incorporated into the fiber as an emitter. Resonant modes were identified using Mie theory, and Q values and free spectral range were measured. Subsequently, the electrospun fibers were used to detect streptavidin, and the sensitivity of the PVA/M13 biosensors was measured.

**Results and Discussion:** The surface of the near-field electrospun PVA/M13 fibers was smooth and featureless, suitable for optical resonators. Furthermore, M13 were present on the fiber surface with affinity for streptavidin intact. With the incorporation of the dye R6G, sharp periodic peaks were observed that corresponded to the presence of WGM resonances. To demonstrate biosensing, PVA/M13 fibers and control PVA fibers were

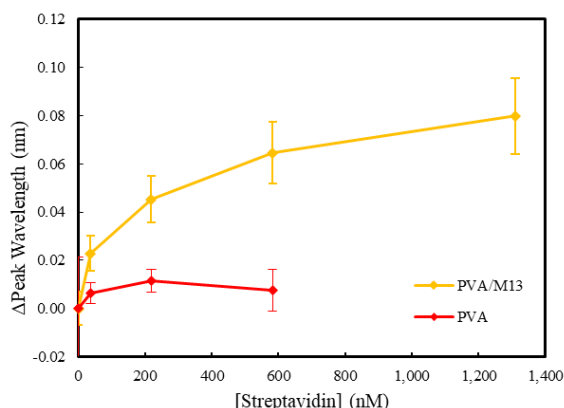


**Figure 1.** Representative WGM peak shift of PVA/M13 and PVA fibers at different streptavidin concentrations

exposed to increasing concentrations of streptavidin solution.

**Figure 1** illustrates the increase in peak wavelength with increasing streptavidin concentration. The shift was attributed to an increase in refractive index caused by streptavidin binding to the fiber surface. PVA/M13 fibers demonstrated a ~8 fold larger shift compared to PVA. This was attributed to the presence of M13 at the surface specifically binding to streptavidin significantly increasing the sensitivity of the electrospun PVA/M13 fiber.

**Conclusions:** These results demonstrate the first report of an electrospun WGM biosensor with a virus bioreceptor. The development of a one-step scalable fabrication for label-free biosensing has the potential for new more efficient biosensors.

**Acknowledgments:** This material is based upon work supported in part by the National Science Foundation under Grant No. ECCS-1406795.

**References:** 1 J. E. Cheeney, S. T.-C. Hsieh, N. V. Myung and E. D. Haberer, *Nanoscale*, 2020, **12**, 9873–9883.

# A Pneumatic Random-Access Memory for Controlling Soft Robots

Shane Hoang<sup>1\*</sup>, Konstantinos Karydis<sup>2</sup>, Philip Brisk<sup>3</sup>, William Grover<sup>1</sup>

<sup>1</sup>Department of Bioengineering, University of California, Riverside, CA, USA

<sup>2</sup>Department of Electrical and Computer Engineering, University of California, Riverside, CA, USA

<sup>3</sup>Department of Computer Science and Engineering, University of California, Riverside, CA, USA

**Introduction:** Pneumatically-actuated soft robots have advantages over traditional rigid robots in many applications. In particular, their flexible bodies and gentle air-powered movements make them more suitable for use around humans and other objects that could be injured or damaged by traditional robots. However, existing systems for controlling soft robots currently require dedicated electromechanical hardware (usually solenoid valves) to maintain the actuation state (expanded or contracted) of each independent actuator. When combined with power, computation, and sensing components, this control hardware adds considerable cost, size, and power demands to the robot, thereby limiting the feasibility of soft robots in many important application areas.

**Materials and Methods:** In this study, we introduce a pneumatic random-access memory (RAM) that uses air to set and maintain the states of large numbers of soft robotic actuators (using a demultiplexer design) without dedicated electromechanical hardware. These pneumatic logic circuits use normally-closed microfluidic valves as transistor-like elements; this enables our circuits to support more complex computational functions than those built from normally-open valves. We perform proof-of-concept experimental testing of our pneumatic RAM by using it to control soft robotic hands playing individual notes, chords, and songs on a piano keyboard.

**Results and Discussion:** We demonstrate an eight-bit nonvolatile RAM that can maintain the states of multiple actuators, control individual actuators and multiple actuators simultaneously using a pneumatic version of time division multiplexing (TDM), and set actuators to any intermediate position using a pneumatic version of analog-to-digital conversion. Shown in Figure 1 is a demonstration of the pneumatic memory, with four soft robotic fingers being controlled by the pneumatic RAM. Once the first finger has been contracted, operations of the chip are routed to the three other fingers while the first finger remains actuated due to the trapped vacuum within it.

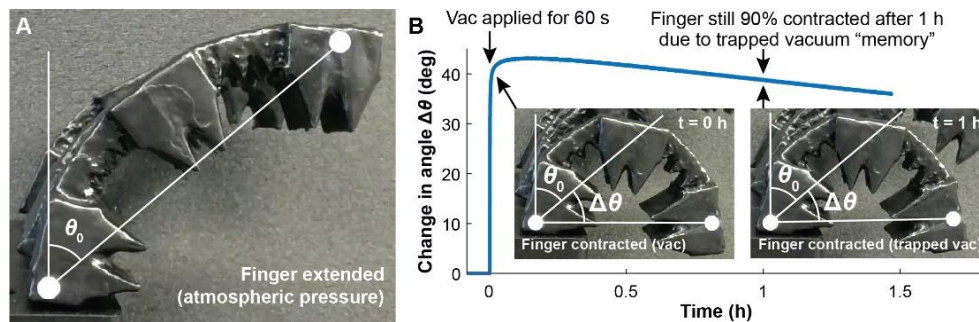


**Figure 1.** Measuring the amount of time that the pneumatic RAM can “remember” the value of a Memory bit (and how long a soft robotic finger connected to the Memory bit can maintain its actuation state). (A) At atmospheric pressure, the finger has a natural curve with an angle  $\theta_0$ . (B) At time = 0, the pneumatic RAM applies vacuum the finger for an excessively-long 60 s, which causes the finger to contract an additional  $\Delta\theta$  degrees. After 60 s the pneumatic RAM disconnects the input vacuum from the finger, which remains contracted due to the vacuum trapped inside the finger. For the next hour, the pneumatic RAM cycled through these three fingers, contracting and extending one every ten seconds. Even though the pneumatic RAM chip's operation introduces small amounts of atmospheric-pressure air to the first finger, the finger nonetheless remained 90% contracted 1 h after the applied vacuum was removed.

**Conclusions:** In this work, we introduced a pneumatic nonvolatile random-access memory (RAM) and showed that this pneumatic logic circuit can dramatically reduce the amount of peripheral hardware required to control a soft robot. Through the use of the demultiplexer and the capability of the pneumatic RAM to remain contracted for 1 hour before requiring its state to be refreshed, it becomes possible to control a much more complex system of soft robots using a minimal amount of electronic hardware. Not only does this minimize the cost required to control and maintain these robots, it also presents soft robots as a viable alternative to traditional hard robots, capable of complex operations in situations where safety can be compromised from rigid bodies or sparks in hazardous areas.

# Characterization of Microenvironmental Changes to the Bone Marrow after Cytotoxic Conditioning

Nastaran Abbasizadeh<sup>1,2\*</sup>, Joel. A. Spencer<sup>1,2,3</sup>

<sup>1</sup>Department of Bioengineering, School of Engineering, UC Merced, Merced, CA, USA

<sup>2</sup>NSF-CREST Center for Cellular and Biomolecular Machines, UC Merced, Merced, CA, USA

<sup>3</sup>Health Science Research Institute, UC Merced, Merced, CA, USA

**Introduction:** Hematopoietic cell transplantation (HCT) remains an important treatment for hematologic malignancies. A key factor for successful HCT is the cytotoxic preconditioning required to reduce the burden of malignancy, suppress the host immune system, and enable engraftment and tolerance of the donor hematopoietic cells. It is known that conditioning regimens invariably damage the tissues where donor cells engraft (e.g., bone marrow (BM)), but there remains a knowledge gap of how these regimens change these tissues over time and how those changes affect the recovery of the hematopoietic and immune systems. In this project, we aim to characterize the microenvironmental alterations to the BM (e.g., oxygenation, hemodynamics, and vascular remodeling) over time after cytotoxic conditioning regimes used to treat hematologic malignancies.

**Materials and Methods:** Using two-photon intravital and *ex vivo* microscopy, we directly visualized the microenvironmental changes to the BM niche of C57BL/6J mice longitudinally (days 2, 5, and 42) after busulfan (BU) treatment. The chemotherapy administration was applied under both reduced intensity (RIC) and myeloablative (MAC) conditionings using intraperitoneal injections of 40 mg/kg and 80 mg/kg busulfan, respectively. Mice were then transplanted with  $1 \times 10^6$  whole bone marrow stem cells from a UBC-GFP donor mouse. During live imaging, Rhodamine-B-Dextran (70 kDa) was injected retro-orbitally to visualize blood vessels and measure vessel permeability. For *ex vivo* imaging of the long bone, Alexa647 conjugated antibodies against CD31, CD144, and Sca-1 were injected 30 min. ahead of intracardiac perfusion. Harvested long bones were frozen and shaved using a cryostat to enable visualization of the BM microenvironment.

**Results and Discussion:** *Ex vivo* imaging of the long bones revealed a decrease in the vessel density and abnormal vascular structure on Days 2 and 5 due to endothelial damages and then recovery by Day 42 (Fig. 1). Intravital imaging of the calvarial bone marrow indicated that vascular leakage significantly increased in the calvarial BM of BU treated mice at all timepoints (data not shown). Despite cytotoxic damage to the BM microenvironment, preliminary imaging and chimerism studies indicated a noticeable difference in number and distribution pattern of donor BM cells in BU treated mice compared to control.

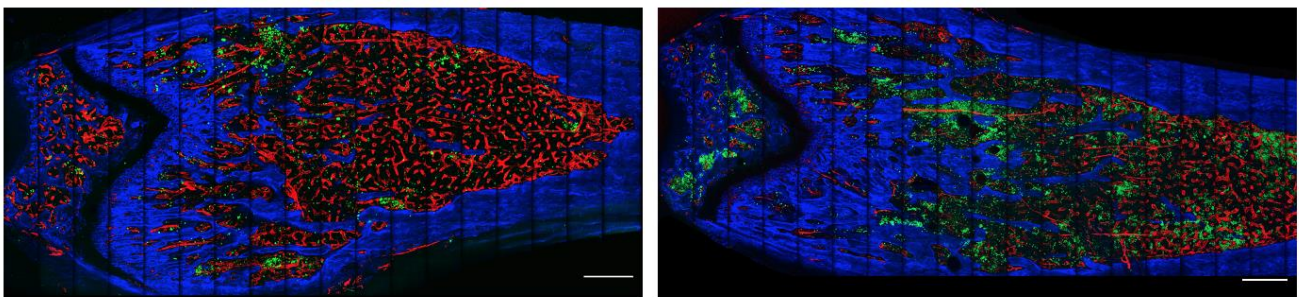


**Figure 1:** *Ex vivo* long bone images of a) Control b) BU-treated mice 5 days after transplantation with  $1 \times 10^6$  Ub-GFP hematopoietic cells, Blue: Bone (SHG: Second Harmonic Generation), Green: Ub-GFP hematopoietic cells. Scale bars  $\sim 200 \mu\text{m}$

**Conclusions:** This study reveals details of the alterations in the BM niche over time after cytotoxic treatment, and the role that these alterations play in the recovery of the hematopoietic system after HCT in both MAC and RIC conditionings.

**Acknowledgement:** Funding support was provided by the UC Cancer Research Coordinating Committee (C21CR2189).

## Cell Detection in the Cleared Thymus using Machine Learning

Shreya Shriram<sup>\*1</sup>, Kumaran Akilan<sup>1</sup>, Christian Burns<sup>1</sup>, Joel A. Spencer<sup>1</sup>

<sup>1</sup>Department of Bioengineering, University of California, Merced, CA

**Introduction:** The thymus plays a critical role in the adaptive immune system as the primary site of T-cell maturation. In particular, the utilization of whole organ imaging to study the mouse thymus will provide key insight into the adaptive immune response and how thymocytes repopulate and develop into mature T cells. However, the proliferation of tissue clearing techniques and whole organ microscopy has resulted in increasingly larger and more unwieldy biological image datasets. With large datasets comes the need for large scale data processing, which until recently has relied heavily on manual or semiautomated methods. In the thymus in particular, manual cell labeling has been limited by human perception and bias. Machine learning has shown great promise in automating the cell detection and classification while maintaining objectivity and consistency and increasing data turnover. In this study, we train a supervised machine learning model using classification and regression algorithms to accurately label thymus progenitor cells.

**Materials and Methods:** Whole cleared thymi containing transplanted GFP-labeled thymocytes were imaged using two-photon microscopy and used for training and validation. Training the machine learning model was split into two parts – (1) recording and processing an image stack, and (2) training the classifier. We begin by using color leaf filtering and gaussian noise reduction to filter the stack and isolate cell candidates by identifying pixel clusters. With feature extraction, we are then able to record different aspects of each cell candidate such as cell size, density, hue, saturation, and value variance. We trained our model with a total of fourteen features and compared four different algorithms – Adaboost, Random Forest, Elastic Net Regression, and Lasso Regression. The algorithm's hyperparameters and statistical processes were iteratively modified to increase the model's effectiveness. We measured model efficacy based off two parameters – accuracy and ROC-AUC. The accuracy is the percentage of correctly labeled cells, while ROC-AUC is a comprehensive metric of the model's accuracy combined with its rates of type 1 and type 2 error.

**Results and Discussion:** Based on preliminary testing of our model, we were able to get about 80-85% accurate labeling of cell candidates with an ROC-AUC between 0.89 and 0.95. The Adaboost algorithm is generally on par with Random Forest in accuracy, while Random Forest consistently outperforms Adaboost in its ROC-AUC. Additionally, based on our backward selection process, cell candidate's cell density is the most contributing factor to labeling cells.

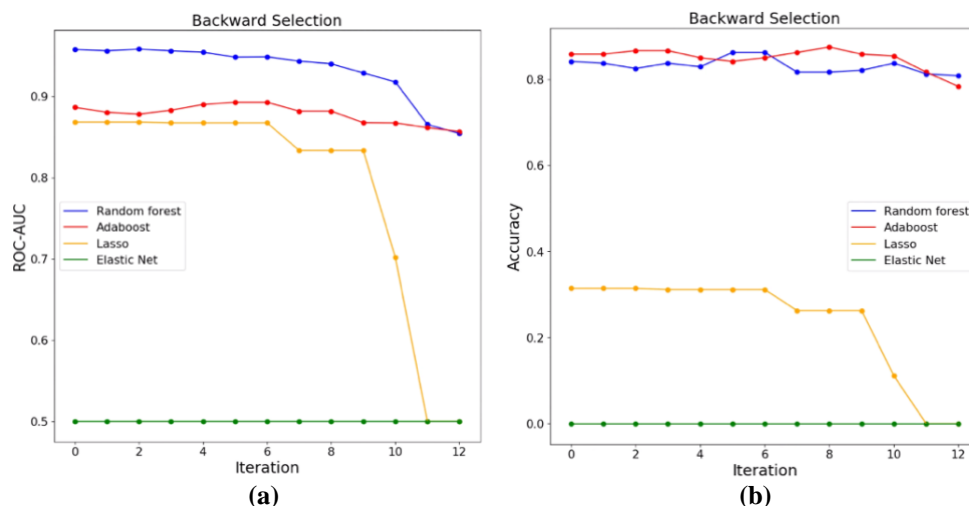


**Figure 1.** Respective ROC-AUC (a) and Accuracy (b) of each algorithm at each iteration of backward selection.

**Conclusion:** Of the four algorithms we've trained and tested, the two most promising are the Adaboost and Random Forest classifiers, which are based on ensemble learning methods. Moving forward, we plan to improve the performance of these machine learning models and to apply them to new thymus imaging datasets.

**Acknowledgements:** Funding support was provided by NSF-CREST (NRF-HRD-154748). We want to thank Drs. Karin Gustafsson and David T. Scadden for providing the thymus samples for imaging.

## Tissue Heat Transfer During Cardiac Radiofrequency Ablations

Karcher Morris\*, Shengfan Hu, Matthew Kohanfars, Frank E. Talke

Center for Memory and Recording Research, Jacobs School of Engineering, UC San Diego

**Introduction:** Cardiac ablation procedures are commonly performed to treat atrial fibrillation. Cardiac electrophysiologists often use radiofrequency (RF) ablation catheters to thermally ablate (or burn off) defective heart tissue causing the fibrillation. During ablation, the esophagus may be in contact with the heart. The heat generated by RF can transfer to the esophagus and cause thermal lesions or, in a rare worst-case, atrioesophageal fistula. For this clinical problem to be properly addressed, it is important to understand and measure the tissue heat transferred to the esophagus.

**Materials and Methods:** Our research team has developed an Esophageal Deflection Device (EDD) to move the esophagus away from the heart during cardiac ablation procedures. We recently developed a silicone skin with embedded thermistors to monitor temperature on the inner esophagus wall during ablation. An experimental setup was created using excised esophageal and atrial porcine tissue to test the temperature-sensing silicone skin with a 5x3 sensor grid. To complement this experimental study, a finite element model was developed to simulate the heat transfer under these conditions. Temperature profiles were simulated as a function of time, input parameters and boundary conditions.

**Results and Discussion:** Experimental results were captured for the 15 thermistor silicone skin as a temperature-defined heat source of 55 °C was applied to the inner atrial side of the layered atrial/esophageal tissue. Figure 1 illustrates a typical experimental result. A finite element model, comprised of the same tissue layers, was developed and simulated. A typical numerical result is shown in figure 2. After 60 seconds, the maximum temperature on the inner esophagus wall rose to approximately 42°C and 46 °C for the experimental and simulation results, respectively. Sensor spacing was found to be a very important parameter for the sensing of a temperature rise on the inner esophagus wall. Through the numerical simulation, a large temperature difference was found between the inner and outer esophageal walls. This result emphasizes the importance of adequate temperature sensing along the inner esophagus wall to protect the esophagus from thermal damage.

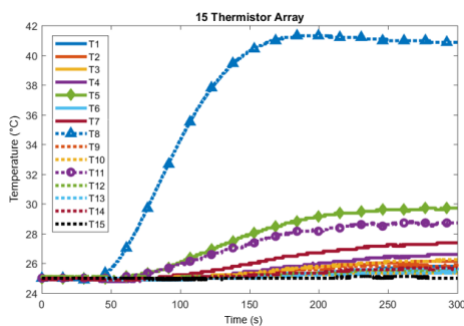


**Figure 1.** Experimental result illustrating temperature sensor rises on a silicone sheet 15 thermistor array.

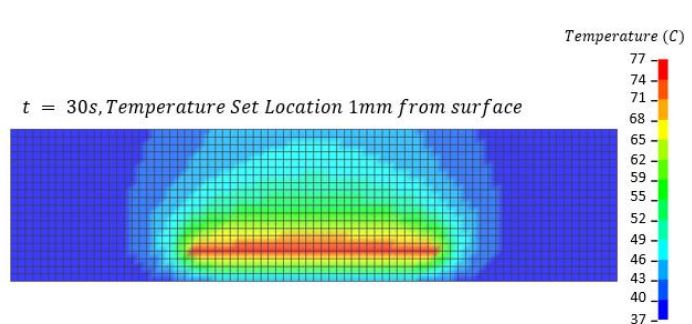


**Figure 2.** Numerical simulation result using LS Dyna transient solver.

**Conclusions:** Experimental and numerical analysis of heat transfer through heart and esophagus tissue has provided useful information in terms of evaluating a silicone sensor skin. This model assisted our research in understanding how temperatures measured on the inner esophagus can relate to temperature at various depths between the inner esophagus wall and the inner atrial wall.

**Acknowledgements:** Significant support was provided by Dr. Greg Feld and Dr. Thomas Savides at UC San Diego's School of Medicine and Jacobs Medical Center. The two medical doctors have shared this problem with us and worked with us on both fully understanding the problem and working toward a meaningful solution.

## Portable Ophthalmic Instrument for Remote Self-Examination During COVID-19

Alex Phan\*<sup>1</sup>, Buu Truong<sup>1</sup>, Benjamin Suen<sup>1</sup>, Gerrit Melles<sup>2</sup>, Frank E. Talke<sup>1</sup>

1. Center of Memory and Recording Research (CMRR), UC San Diego
2. Netherlands Institute for Innovative Ocular Surgery (NIIOS)

**Introduction:** Currently, standard care in ophthalmology monitors patient eye health through routine follow-up phone calls or in-person office visits. While in-person office visits allow physicians to directly assess the eye health of a patient, routine follow-up phone calls often do not provide sufficient information to determine if an office visit is necessary. This results in many unnecessary office visits and limits the patient to infrequent monitoring that can only be performed in-person. As the 2020 COVID-19 pandemic continues to pose challenges for public health, social distancing guidelines and restricted closed-door environments increase the need for the elimination of unnecessary office visits in lieu of at home examinations. In this paper we report on the design and testing of a multi-functional ophthalmic device for remote eye examinations.

**Materials and Methods:** The device integrates two standard examination instruments typically used in-clinic to assess the eye health of a patient, i.e., the slit lamp and the visual acuity tester. The slit lamp mode projects a sweeping slit of light onto the anterior chamber of the eye. The patient simply positions the ophthalmic device in front of the eyes and begins with the examination using a button-controlled interface. Physicians can view the patient's eye live remotely or access the results from the self-examination later using images and video recordings. The visual acuity mode allows patients to test their visual acuity through a series of images similar to those on a so-called "Snellen" chart. More importantly, the device allows the patient to perform the exam without a secondary person or trained technician. The off-the-shelf optical and electrical components are fitted within a compact design and 3D printed casing to allow for ease of handling. We conducted preliminary tests of the ophthalmic device and showed results from slit lamp and visual acuity examinations of ten patients.

**Results and Discussion:** All ten patients were able to perform self-examination using the portable ophthalmic device following a short training. Fig. 1 shows a set of images obtained from a typical slit lamp self-examination by the patients. The integration of the rotating mirror enabled the slit beam to automatically sweep across the anterior segment providing the physician a complete view of the eye. Optical cuts into the cornea, the iris and the crystalline lens are visible with high clarity. The quality of these images is similar to that of images obtained using a conventional slit lamp.

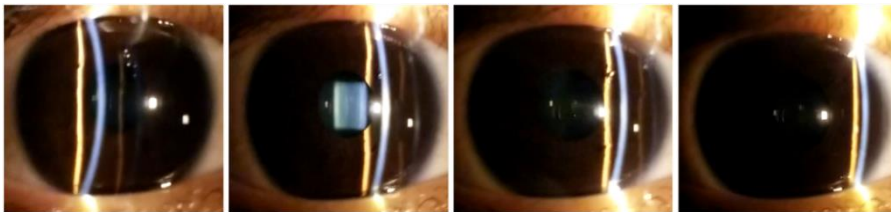


**Figure 1.** Images obtained from a typical slit lamp self-examination.

The patients also performed the visual acuity test by themselves successfully. Results from seven patients showed equivalent visual acuity levels between the self-test and conventional method. Results from the other three patients showed a difference of one Snellen level compared to in-clinic testing. We hypothesize that these minor differences in visual acuity results observed may be due to the differences in the contrast of each letter when viewed on an LCD screen as compared to when the letters are viewed on a conventional chart. Aberrations caused by the lens system may also affect the testing outcomes.

**Conclusions:** The user-friendly device is a "clinic in a box" that addresses the accessibility challenges related to complex instruments that can only be used in the clinic by trained professionals. Ultimately, the device connects patients to physicians in their own home and promises to be a great improvement in ophthalmic care.

## Precise control of immune modulation using DNA scaffold-mediated biomaterial functionalization

Authors: Xiao Huang\*, Jasper Z. Williams, Ryan Chang, Wendell A. Lim, Tejal A. Desai  
University of California, San Francisco, CA 94158

A high level of control over the surface functionalization of biomaterials is essential for immune cell modulation. Here, we developed biocompatible immune cell engaging particles (ICEp) that use synthetic short DNA as scaffolds for efficient and tunable protein loading. To improve the safety of chimeric antigen receptor (CAR) T cell therapies, micron-sized ICEp were injected intratumorally to locally activate systemically administered AND-gate CAR-T cells. ICEp presenting a high density of priming antigens, difficult to achieve by other chemistries, offer advantages in activating engineered human and murine immune cells. The ratiometric control of costimulatory ligands (anti-CD3 & anti-CD28 antibodies) and the surface presentation of a cytokine (IL-2) on ICEp were shown to significantly impact human primary T cell activation phenotypes.

**Introduction:** Immunomodulatory signals such as costimulatory ligands, cytokines, antigens, and checkpoint inhibitors have been used extensively to improve the efficacy and safety of immunotherapies. Synthetic biocompatible materials have been employed as carriers for these biomolecules to facilitate specific localization and prolonged stability *in vivo*. However, there is an unmet need for robust and biocompatible conjugation strategies to surface-functionalize biodegradable materials with multiple moieties (e.g. proteins/antibodies) at a high level of control. The achievement of high tunability of biomaterials functionalization would significantly advance the needs of cell modulation in immunotherapies.

**Materials and Methods:** Herein, we developed short synthetic DNA scaffolds for the functionalization of proteins or antibodies on the surface of biodegradable particles (Fig. 1A)<sup>2</sup>. A series of optimization studies were carried out to achieve maximum loading density, ratiometric control of moiety loading, adaptability to different particle sizes/composition, and feasibility for *in vivo* use. For our demonstration platform, we fabricated micron-sized particles using a biocompatible poly(lactic-co-glycolic acid) (PLGA) polymer. Particles presenting immunomodulatory signals with precise density and ratio control (Fig. 1B,C) were then tested the impact to the activation of human primary T cells and engineered AND-gate CAR-T cells.

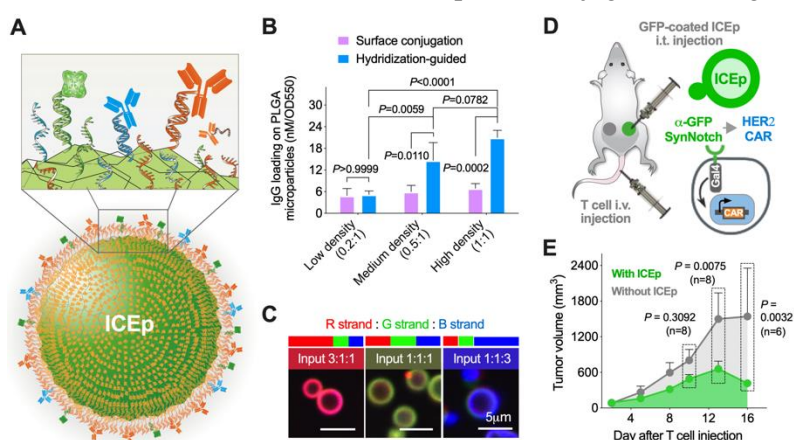


**Figure 1.** A) Schematic of biocompatible particles presenting therapeutic proteins via surface DNA scaffolds. B) High and controlled density of IgG on particle surfaces. C) Precise ratiometric control of surface DNA scaffolds and functional moieties. D) Schematic of the NSG mice two tumor model for selected clearance by ICEp-primed synNotch CAR-T cell activation. E) Tumor growth curve of T cell and ICEp treated mice in D.

**Results and Discussion:** We found increasing ratios of anti-CD3 to anti-CD28, 1:5, 1:3, 1:1, 3:1 to 5:1, on microparticles yielded a linear increase of *ex vivo* expansion of primary human CD4<sup>+</sup> and CD8<sup>+</sup> T cells until reaching a plateau at 3:1 ratio. For CD8<sup>+</sup> T cells, the ratio of 3:1 resulted in the highest percentage of central memory cells,  $51.4 \pm 7.2\%$  vs.  $14.4 \pm 7.6\%$  for 1:5 ratio ( $n = 5$  donors). Particle surface presentation of IL-2 using an anti-IL-2 antibody (*in trans* to CD3/28 particles) yielded ~3 fold more *ex vivo* expansion of CD4<sup>+</sup> and CD8<sup>+</sup> T cells in 14 days when compared to the equivalent dose of soluble IL-2. Using intratumoral injection of microparticles presenting a ligand for a synthetic Notch receptor, we locally induced chimeric antigen receptor (CAR) expression on systemically infused engineered T cells and observed CAR T cell killing of the injected tumors, while sparing the uninjected identical tumors in the contralateral flank (Fig. 1D,E). These results highlight the potential of this platform in achieving better control of therapeutic cell manufacture and local tuning of immunotherapies. Ongoing work is using DNA origami-mediated patterning to dissect spatial requirements of various T cell activating ligands to better understand critical parameters of T cell activation with the goal to improve the design of immunotherapies.

**Reference:** 1. Huang X, Williams JZ, Chang R, Li Z, Burnett CE, Hernandez-Lopez R, Setiady I, Gai E, Patterson DM, Yu W, Roybal KT, Lim WA, Desai TA. DNA scaffolds enable efficient and tunable functionalization of biomaterials for immune cell modulation. *Nature Nanotechnology*, 16, 214-223 (2021).